Mechanical Systems and Signal Processing 139 (2020) 106615

Contents lists available at ScienceDirect

Mechanical Systems and Signal Processing

journal homepage: www.elsevier.com/locate/ymssp

Traction-based multi-scale nonlinear dynamic modeling of bolted joints: Formulation, application, and trends in micro-scale interface evolution

Nidish Narayanaa Balaji [a], Wei Chen [b], Matthew R.W. Brake [a,*]

[a] Department of Mechanical Engineering, Rice University, Houston, TX 77005, United States
[b] School of Aerospace Engineering and Applied Mechanics, Tongji University, Shanghai 200092, PR China

ARTICLE INFO

Article history:
Received 15 July 2019
Received in revised form 29 October 2019
Accepted 3 January 2020

Keywords:
Frictional systems
Rough contact
Zero thickness elements
Surface characterization
Bolted joints
Multi-scale modeling

ABSTRACT

A new framework for modeling the dynamics of bolted structures is proposed that considers the nonlinear interfacial modeling of bolted structures using multi-scale traction-based contact constitutive laws implemented through Zero-Thickness Elements (ZTE). Using rough contact theory, it is possible to establish fundamental constitutive relationships with parameters estimated from micro-scale surface scans. Such a model is employed in the framework for a three bolt lap-joint benchmark (the so-called "Brake-Reuß-Beam"). Since the characterization of the interface is conducted in a full-field manner on top of a finite element mesh, the framework is also demonstrated to be applicable for conducting full-field micro-scale interface evolution studies. Preliminary studies are conducted to establish correlations of local changes in relevant roughness parameters with predicted local tractions and dissipation fluxes.

1. Introduction

Developing a definitive understanding of the dynamical behavior of jointed systems can be significantly enabling for design engineering [1]. The interfacial phenomena in a jointed connection can be highly nontrivial, and physical insight in a fundamental level is of utmost importance for predictive modeling. Dealing primarily with bolted joints, the current work focuses on modeling such systems in a physically consistent manner, placing emphasis on assessing the predictive capabilities of the developed model.

Just the static loading condition of a bolted joint has been demonstrated to be highly variable due to uncertainties associated with the torque-tension relationship [2–5]. Furthermore, even for a given level of bolt tension, the lack of consensus in a reasonably accurate contact model complicates the prediction of the pre-stress configuration (see discussions between compliant and "hard" contact, such as [6]).

Static considerations aside, it has been experimentally demonstrated that bolted interfaces experience very rich kinematic phenomena in dynamic excitation [7–9], which makes it necessary for any predictive approach to have sufficient fidelity in interfacial representation. Moreover, the contact interface is governed by highly nonlinear mechanics, ranging from plastic flow and damage [10,11] to asperity fractures and adhesion [12,13]. However, accounting for all of these would result

* Corresponding author.
E-mail addresses: nb25@rice.edu (N.N. Balaji), meshiawei@tongji.edu.cn (W. Chen), brake@rice.edu (M.R.W. Brake).

https://doi.org/10.1016/j.ymssp.2020.106615
0888-3270/

in a model that would be nearly infeasible for practical deployment. It is thus of relevance to determine the most significant underlying physics that can provide sufficiently accurate predictions while still retaining low computational complexity.

From a modeling standpoint, since the study of pre-stress and interfacial friction are geared toward different objectives, it is sometimes thought that it is admissible to decouple the static simulation and the dynamic simulation [14,15]. In such studies, the conventional approach is to first conduct a static simulation for the prestress state and then the dynamic analyses are applied in the sense of perturbations about this state. However, as will be shown in the current work, this approach has a significant disadvantage in that it defeats the purpose of applying physically derived nonlinear contact models, especially those pertaining to normal contact.

In order to model the contact behavior, it is common practice among phenomenological models to consider the normal and the tangential behavior separately or to only allow for one way coupling (i.e., the tangential behavior does not affect the normal behavior, but at the same time is dependent on it) [16,17]. From a mathematical standpoint, the contact problem, more formally referred to as the Signorini problem [18], is formulated as a variational inequality (see [19] for details). However, the inequality problem can be expressed easily only for infinitely smooth surfaces, while most real surfaces have roughness, modeled usually as randomly distributed micro-scale asperities on the surface [20]. Models of the response of such surfaces may be achieved either by creating an exact computational representation of the interface by modeling each asperity and solving the Signorini problem here or by developing compliant models accounting for the statistical distribution of asperities [21]. Owing to the magnitudes of length-scales involved (asperities in the order of μm and components in the order of milli- and/or centi-meters), the former approach tends often to be computationally prohibitive and thus has very limited applicability in a system-level framework. The latter approach, is computationally cheaper, while at the same time capturing the effects of the surface asperities in a statistically averaged sense. There exist many such formulations for the normal contact, for instance the linear penalty stiffness approach as in [22,23] and the nonlinear penalty models in [24]. Some of these studies have also been used to account for plastic flow in the asperity level [25], leading to considerably improved dissipative compliant models.

For the tangential behavior, physical observations of "stick" and "slip" have traditionally been used to derive independent phenomenological models (see [26] for a review of some of the earliest efforts). These are usually modeled as discrete sliders with a finite elastic limit, formally known as Prandtl-Ishlinskiĭ models [27] (consisting of plays [28] and/or stops or Jenkins elements [29]), which form the basis of some of the most popular elastic dry friction models in use today [14,30,31]. There have been several reconciliations between the parameters involved here and surface roughness (see, for instance, [22,23,32–35]). Infinite distributions of these discrete elements lead to the formulation of the Iwan models [36] (first proposed for plasticity), which have gained significantly in popularity since the four-parameter Iwan model was proposed in [37]. However, the drawbacks with applying the latter approach in the current work is twofold: first, the non-uniform and unsteady pressure distribution in the interface (see [7–9], for some experimental studies) during dynamical operation makes them inapplicable for the test problems currently considered; and second, reconciling the involved parameters with the surface roughness is not as direct as for the former.

1.1. Overview of modeling approach

The current work proposes a physically congruent structural dynamics modeling framework that attempts to tackle each of the above issues. Experimentally, following the procedure in [5], bolt tensions are applied in a controlled manner by monitoring the axial strains developed in the bolts so that the bolt loading conditions are specified without having to resort to approximated torque-tension relationships.

The interface is represented using Zero-Thickness Elements [38] (ZTEs) so that the model is capable of representing local interfacial kinematics sufficiently well. Adjustments for meso-scale irregularities in the topology of the surface are employed so that machining imperfections (such as waviness) may be accounted for. A compliant rough contact model is formulated using parameters estimated from surface scans for modeling the interfacial mechanics. The model involves the macro-scale model, meso-scale imperfections, and the micro-scale asperities in one-way relationships, i.e., the lower length-scales influence the higher ones (micro- and meso- influencing the macro-), while the vise-versa is not explicitly captured in the model (but explored in a post hoc fashion). Interfacial scans are conducted before and after dynamical testing in order to attempt at establishing statistical correlations between predicated interfacial tractions and dissipation fluxes to changes in surface roughness parameters. The purpose is to establish surface scanning as a possible independent verification of the developed contact model(s).

A coupled modal quasi-static approach is formulated in the spirit of the QSMA approach in [15,39]. The main motivation for this is in order to for it to be possible to employ fully non-linear contact models without making assumptions beyond the ones necessary for QSMA. It was observed in [40] that the prestress analysis preceding the dynamical analysis influences the nature of the response in very undesirable ways. The coupled QSMA is formulated so as to not encounter such issues in practice.

It must be noted here that the above approach does not model modal interactions and still assumes that the modal forcing may be taken to remain approximately constant throughout the operational regime (as in QSMA). If a more detailed understanding of the steady state dynamical behavior of the structure is sought, one must opt for time-domain (shooting, direct integration, etc.) or frequency domain (harmonic balance) methods, which are both several orders of magnitude more expensive than the current approach.

The experimental dynamic characterization in this work involves the identification of effective nonlinear modal characteristics from ring down data extracted from impact hammer tests using a fairly recent approach [41,42]. Since the nonlinear modal modeling approach predicts these quantities directly, a physically meaningful comparison may be made between model prediction and experimental observations.

In what follows, section 2 describes the interface representation (section 2.1) and modeling (section 2.2) followed in the current work. Section 3 describes the benchmark structure (section 3.1) and interfacial parameter identification (section 3.2). The results of the benchmark investigation for the dynamic tests the surface roughness evolution studies are presented in section 4. And Section 5 provides key discussions, conclusions, and the outlook the authors take at the end of the study.

2. Interface modeling

In order to model the interface, two things must be established: how the interface is represented, and how its mechanical behavior (response to kinematic phenomena) is defined. Zero-Thickness Elements (ZTE), occurring first in [38], are used to represent the contact interface. The implementation using traction-based compliant models [14,43] and super-convergent-nodal recasts is described in section 2.1. The 3D nonlinear contact model used is adapted from [21,32] for the normal and from [44–46] for the tangential contact relationships. The surface friction concept has been adapted and slightly modified from [47], where it was applied for a phenomenological model. Classical results, as some of these may be, have, as far as the authors' knowledge, not been applied to model bolted joints in the current spirit. All of the constitutive laws are formulated using empirical asperity distributions in each discretized element on the interface, through which element-wise traction-displacement laws are established (see section 2.2). Here, the word traction is used to refer to the surface traction vector (see Cauchy's stress theorem [48]). No assumptions are made with regards to the actual distribution of the asperities.

It must be noted that ZTE's may be used only for small displacement applications, which is the expected case for tightly bolted joints such as the Brake-Reuß Beam benchmark (BRB) [49]. This gives the ZTE approach a significant computational advantage since contact-searches are completely avoided in the formulation. For applications with larger displacements, there exist more general approaches (see, for instance [50]) involving contact and closest point searches (usually resulting in computationally burdensome implementations).

As a natural requirement of element-based modeling, it is necessary to describe the continuum behavior of each element to relative distortions. Thus, traction-based nonlinear constitutive relationships need to be employed in such a way as to consistently calculate nodal forces by assembling traction-integrals across the elements in the interface. One of the main advantages of element-traction approaches is that the model may be consistently employed for arbitrarily shaped meshes in interfaces. Note that the same may not be said about node-to-node contact models [51], which are limited in their applicability for irregular or biased mesh scenarios. This requirement is particularly germane for bolted interfaces, where the presence of the holes makes the mesh highly irregular.

Cheap computational implementation of these models may be achieved by evaluating the nonlinear traction vectors at a set of quadrature locations (extracted using interpolation matrices computed offline) in each element and using appropriate weights to integrate them with the corresponding shape functions (achieved with an integration matrix, also computed offline) to obtain the integrated effects (forces and Jacobians/stiffnesses) as nodal forces and stiffnesses to be used by the solver. This offers an implementation that is cheap, yet consistent with the weak form that finite element theory is formulated to solve.

2.1. Zero-thickness elements

Fig. 1 depicts a schematic view of an interfacial element with numbered nodes. In the figure, nodes 1-2-3-4 form an element that belongs to one body; 5–6-7–8 belong to another; and the ZTE establishes an "interfacial element" as a combination of these nodes. Being defined as interfacial elements, the nodes in each element are taken to be fixed through the operation. In other words, the mesh (nodal connectivity of the elements) is taken to be fixed throughout the simulation. As noted already, this is a simplification that can be made only for small tangential relative displacement applications (in the $(\xi - \eta)$ plane). A similar but slightly different implementation involves thin-layer elements [52–54], which enforce a small but finite thickness in each element in order to regularize rigid contacts. The zero thickness elements on the other hand, are better suited for compliant contact implementations. The tangential plane natural coordinate axes are ξ, η and the normal direction is n. For flat interfaces, relative kinematics in the $\xi - \eta$ plane are completely governed by frictional laws while those in the n direction are governed by normal contact laws. For non-flat interfaces an additional step involving coordinate transformations will be necessary in order to derive corresponding contact relationships since there might not be a nodal Degree-of-Freedom (DoF) that is aligned along the normal direction. In the current study however, since only small relative displacements and initial gaps are investigated, the z-displacement of the nodes is always taken to be along the n-direction.

Although for the quadrilateral-on-quadrilateral element case (as shown above), the resulting interfacial element is an 8-noded element, only the planar shape functions, in the $\xi - \eta$ plane, are used for the kinematic description in each element. Denoting u as some displacement and using the subscripts *TOP* and *BOT* to denote the top and bottom counterparts respectively, the finite element interpolation may be represented in terms of the shape functions N_i (using Einstein summation notation) as

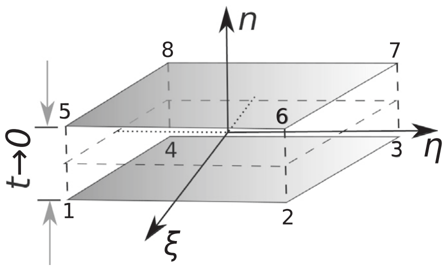

Fig. 1. Schematic of a Zero-Thickness Element (ZTE).

$$\begin{aligned} u_{TOP}(\xi,\eta) &= N_i(\xi,\eta)u^i \quad i=1,2,3,4 \\ u_{BOT}(\xi,\eta) &= N_I(\xi,\eta)u^I \quad I=5,6,7,8. \end{aligned} \tag{1}$$

Eq. (1) represents the interpolation for linear elements, i.e., with each node having the displacements as the Degrees-Of-Freedom (DOFs). The same approach can easily be extended to higher order elements using Hermite shape functions (see [55], for instance, where quadratic elements were used). Using relative coordinates $\Delta u = u_{TOP} - u_{BOT}$, and defining $\Delta u_i = u^i - u^{I(i)}$ by denoting by i and $I(i)$ the top and corresponding bottom nodes, it is possible to represent the kinematics consistently using just the relative DOFs. A convenient framework for expressing the traction non-linearities can be established via

$$\Delta u(\xi,\eta) = N_i(\xi,\eta)\Delta u_i, \tag{2}$$

which is based on just the local relative displacements (see section 2.2 for one particular form). For a structure governed by linear elasticity away from the interface, the corresponding weak form term for a particular displacement-traction pair becomes,

$$\begin{aligned} \mathcal{W}_{int} &= \int_{\Gamma_{TOP}} w_{TOP}(\xi,\eta)t_{TOP}(\xi,\eta)d\Gamma + \int_{\Gamma_{BOT}} w_{BOT}(\xi,\eta)t_{BOT}(\xi,\eta)d\Gamma \\ &= \int_{\Gamma}(w_{TOP}(\xi,\eta) - w_{BOT}(\xi,\eta))t(\xi,\eta)d\Gamma \qquad \text{since} \quad t_{TOP}(.) = -t_{BOT}(.) = t(.) \\ &= \{\Delta w_i\}^T \int_{\Gamma} [N_i(\xi,\eta)]^T t(\xi,\eta)d\Gamma. \end{aligned} \tag{3}$$

Here, $w(\xi,\eta)$ represents the weight functions; $\{w_i\}$ are nodal weight function values, interpolated using the same shape functions $N_i(\xi,\eta)$ (Galerkin projection); and t_{TOP}, t_{BOT} represent the traction fields on the top and bottom faces respectively. The area domains Γ_{TOP} and Γ_{BOT}, taken from the areas of the top and bottom surfaces of the interface, are assumed to have opposite normal directions. This allows for the recast of the sum as an integral of the traction (say, t_{TOP}) over just a single reference domain Γ (taken to be Γ_{TOP} here). Using the variational principle on the weak form, the nodal forces and Jacobians are given by

$$\begin{aligned} \left\{\frac{\partial \mathcal{W}_{int}}{\partial \Delta w_i}\right\} &= \{F_i\} = \int_{\Gamma} \{N_i(\xi,\eta)\}^T t(\xi,\eta)d\Gamma \\ \left[\frac{\partial F_i}{\partial \Delta u_j}\right] &= \int_{\Gamma} \{N_i(\xi,\eta)\}^T \frac{\partial t}{\partial \Delta u} \{N_j(\xi,\eta)\}d\Gamma. \end{aligned} \tag{4}$$

Since there are 3 DOFs per node, the 3 tractions, in general, depend on all 3 DOFs. Numerically, the above integration may be implemented using numerical quadrature, provided that the tractions and their derivatives are known in the quadrature locations. This may be achieved by first evaluating the relative displacements at the quadrature locations, computing the constitutive laws here, and then conducting the weighted summation to integrate and obtain the nodal quantities. The two operations may be computed offline and stored in the form of matrices $\boldsymbol{Q}$ and $\boldsymbol{T}$. Suppose there are N_n nodes and N_e elements with N_q quadrature points per element, $\boldsymbol{Q}$ will be of dimension $(N_eN_q) \times (N_n)$ and $\boldsymbol{T}$ will be of dimension $(N_n) \times (N_eN_n)$. The former is built using just the shape functions evaluated at the quadrature locations while the latter involves the shape functions multiplied by the mapping Jacobi determinant and the quadrature weights for each point. The relevant quantities are thus computed via,

$$\begin{aligned} \{\Delta u\}_{qp} &= \mathbf{Q}\{\Delta u\}_n \\ \{F\}_n &= \mathbf{T}\{t\}_{qp} \\ \left[\frac{\partial\{F\}_n}{\partial\{u\}_n}\right] &= \boldsymbol{T}\left[\frac{\partial\{t\}_{qp}}{\partial\{\Delta u\}_{qp}}\right]\mathbf{Q}^T, \end{aligned} \tag{5}$$

where the subscripts qp and n denote quadrature-point and nodal quantities respectively, with the former being of size N_eN_q and the latter being of size N_n. Since the matrices may be computed offline, the exact computation of the consistent quantities may thus be achieved in an efficient manner by storing these matrices. Different types of elements may be accommodated by considering these during the construction of these matrices, making the approach extensible even to higher order elements in the same fashion.

2.2. Contact model

Since the ZTE formulation requires traction constitutive laws, standard phenomenological models are interpreted in a force-per-unit-area manner localized to each element in order to be applied. This is in contrast to classical phenomenological models, which relate forces to displacements, and to constitutive models, which relate stresses to strains.

2.2.1. Normal contact

It is first assumed that the rough surface may be modeled as a set of ellipsoids of uniform effective radii (planar axes) β (estimated by the mean from measurements) located z distance away from the nominal axis of each surface. The assumption of uniform effective radii is commonly encountered in rough contact literature, starting from [21]. In [22] the average effective radius is used to derive analytical relationships thus establishing force-displacement relationships in each sphere-pair as an integral contact formulation. Fig. 2a shows a schematic of the contact between two bodies with circular profiles. Denoting the distance between the centers in the undeformed and deformed configurations by r_0 and r respectively, the contact area (a) and load (f)-displacement ($w = r - r_0$) relationship in the elastic regime is expressed using the Hertzian solution [56] for this case by

$$\begin{aligned} &a = \pi\beta w \qquad \text{with} \quad w = r - r_0 \\ &f = \tfrac{2}{3}\tfrac{E}{(1-\nu^2)}\sqrt{\beta}w^{3/2}, \\ \text{where,} \quad &\beta = \left(\tfrac{1}{R_1^x} + \tfrac{1}{R_1^y} + \tfrac{1}{R_2^x} + \tfrac{1}{R_2^y}\right)^{-1}. \end{aligned} \tag{6}$$

Here, R_j^q is the radius of the ellipsoid in the q direction (x, y) on surface j $(1, 2)$. Although formulations accounting for possible generic orthotropy can be found in the literature [57], the axes are assumed to coincide with the coordinate/measurement x and y directions in the current study.

Further, even though multiple contact scenarios may be considered (e.g., [56]), the current work only uses Eq. (6), parametrized by average effective radii. To calculate the average traction over an entire element/segment, an asperity peak distribution function $\phi(z)$ is defined for each segment as in [21]. For a segment with N asperities, the number of asperities with heights between z and $z + \Delta z$ is given by

$$n(z) = N\phi(z)\Delta z. \tag{7}$$

Over the range of the asperity heights $z \in [0, \infty)$, the individual contributions of each asperity must be summed up over all of the asperities (in contact) to obtain the behavior of the whole segment. Applying summations to the quantities in eq. (6) yields the sums

$$\begin{aligned} &A \approx \sum_{k\in\mathcal{K}} n(z_k)\pi\beta w_k = \sum_{k\in\mathcal{K}} N\phi(z_k)\pi\beta w_k\Delta z_k, \text{ and} \\ &F \approx \sum_{k\in\mathcal{K}} n(z_k)\tfrac{2}{3}\tfrac{E}{(1-\nu^2)}\sqrt{\beta}w_k^{2/3} = \sum_{k\in\mathcal{K}} N\phi(z_k)\tfrac{2}{3}\tfrac{E}{(1-\nu^2)}\sqrt{\beta}w_k^{2/3}\Delta z_k. \end{aligned} \tag{8}$$

Here the set $\mathcal{K}$ is used to denote the set of asperities with heights z_k that are in contact. Denoting the imposed relative normal displacement with d_n, the reference is defined in such a way that $d_n = 0$ for the case with the tallest peaks just touching. The surface interference δ and the deflection w_k for the asperity with height z_k are given by

$$\begin{aligned} &\delta = z_p - d_n \\ &w_k = z_k - \delta. \end{aligned} \tag{9}$$

In the limit $\Delta z_k \to 0$, the sums in eq. (8) may be transformed to the corresponding Riemann integrals. Furthermore, since only the asperities with peak heights greater than or equal to δ are involved in the contact, the set $\mathcal{K}$ may be described fully by limiting the integrals to $[\delta, \infty)$. Therefore, the integral relationships are

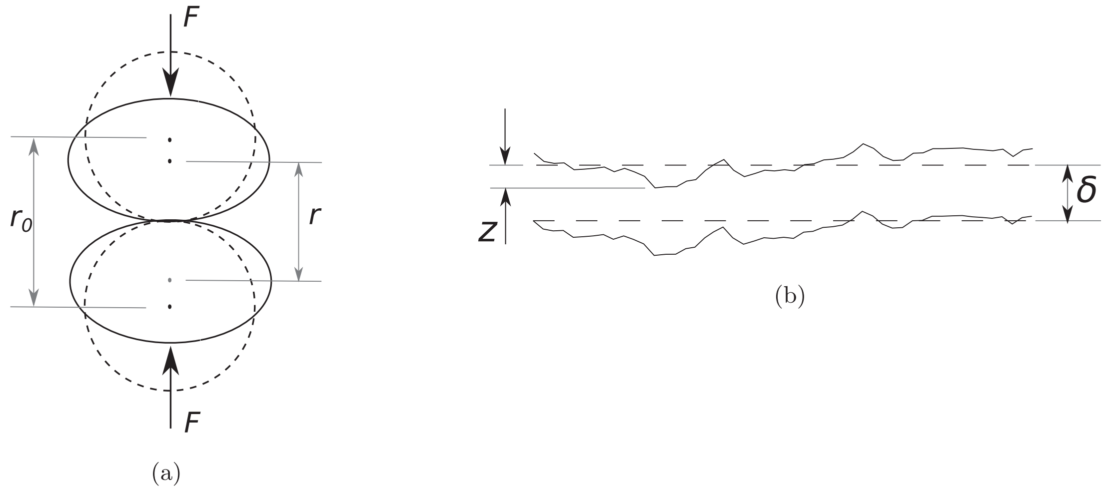

Fig. 2. Normal contact development for rough surfaces: (a) Spherical asperity-on-asperity contact; (b) Contact of rough surfaces.

$$\begin{aligned} A &= N\pi\beta\int_\delta^\infty (z-\delta)\phi(z)dz = N\pi\beta\mathbb{E}[z-\delta|z>\delta] \\ &= N\pi\beta\mathbb{E}\left[z-(z_p-d_n)|z>(z_p-d_n)\right] \end{aligned} \tag{10}$$

$$\begin{aligned} F &= N\tfrac{2}{3}\tfrac{E}{(1-\nu^2)}\sqrt{\beta}\int_\delta^\infty (z-\delta)^{3/2}\phi(z)dz = N\tfrac{2}{3}\tfrac{E}{(1-\nu^2)}\sqrt{\beta}\mathbb{E}\left[(z-\delta)^{3/2}|z>\delta\right] \\ &= N\tfrac{2}{3}\tfrac{E}{(1-\nu^2)}\sqrt{\beta}\mathbb{E}\left[\left(z-(z_p-d_n)\right)^{3/2}|z>(z_p-d_n)\right]. \end{aligned} \tag{11}$$

In the final form of the expression, the term $\mathbb{E}[g]$ denotes the expectation statistic of the term within the square brackets given that z, the asperity heights, are distributed according to the density function $\phi(z)$, and $g(.)$ is some function of z. Mathematically, this is either evaluated through the integral

$$\mathbb{E}[g] = \int_0^\infty g(z)\phi(z)dz, \tag{12}$$

or estimated empirically. A commonly encountered estimator for the expectation statistic is the algebraic average of the function $g(z)$ evaluated over a finite sample population generated from the distribution function given as

$$\widehat{\mathbb{E}}[g] = \frac{1}{N_s}\sum_{i=1}^{N_s} g(z_i), \tag{13}$$

with N_s being the finite sample size. Unless explicitly stated otherwise, the average estimator will be referred to as the empirical estimator henceforth in the current paper.

The effective normal traction t_n^h over an element (or segment) is defined as the force divided by the total area A^e (as opposed to the real contact area in eq. (10)),

$$t_n^h = \frac{F}{A^e} = N\frac{2}{3}\frac{E}{(1-\nu^2)}\frac{\sqrt{\beta}}{A^e}\mathbb{E}\left[\left(z-(z_p-d_n)\right)^{3/2}|z>(z_p-d_n)\right]. \tag{14}$$

The superscript h is used to denote that this is derived from the Hertzian solution for elastic contact.

In the current work, the tractions are integrated over interfacial elements, which means that A^e is the area of the finite element under consideration. This thus requires that the characterization of the roughness of an interface is done on an element-by-element or segment-by-segment fashion so that the local variations in the surface can be modeled appropriately.

For a practical implementation, there are three possible ways of evaluating the traction in eq. (14): (1) Constructing empirical distributions of $\phi(z)$ using surface scans and evaluating the integrals numerically for each displacement value; (2) identifying features in $\phi(z)$ in order to evaluate the statistics using standard results (classical rough contact approaches include formulations for the normal and exponential distribution families); and (3) constructing a table of t_n^h for different δ values and using a curve fit to come up with an approximate model. Of the three, the first is the most accurate, but computationally very expensive for dynamic simulations, and the second is usually not generic enough. The third method would involve conducting simulations at different levels of normal interference (δ) and obtaining corresponding tractions. Although these simulations themselves may be expensive, they need to be conducted just once, since the developed table may be used to obtain a simpler representation of the macro-response after establishing a suitable curve fit. Studies such as [58] and its references develop such approximate models for several standard distribution functions. The current work uses the third approach and is described in detail in section 2.3.

From a computational stand-point, the normal traction is expressed as

$$t_n(u_n) = \begin{cases} t_n^h(u_n) & t_n^h > 0 \quad (contact) \\ 0 & otherwise \quad (separation). \end{cases} \tag{15}$$

Note that since the contact model employed here is based on the Hertzian solution, it is implicitly elastic and thus there is no hysteretic energy dissipation captured in the normal contact. Moreover, as can be seen by the contact condition in eq. (15), the effects of adhesion are not considered in the current model. A common way of modeling adhesion in normal contact is to allow for some finite negative normal traction before complete separation [59]. See section 3.2 for some discussions on this for the current case.

2.2.2. Tangential Contact

Although there exist fully nonlinear rough contact relationships for frictional tangential contact (such as those employed in [25,60]), the current work uses a simplified elastic dry friction element for this. The "stuck" regime is characterized by traction that are linearly proportional to the relative displacements while the "slipped" regime is a constant force along the stuck prediction direction. The formulation is similar to [47], except for the traction-based adaptation and the fact that the stiffnesses are dependent on the normal relative displacement. When fully stuck, the traction developed is given by

$$t_t^{stuck} = k_t u_t. \tag{16}$$

Here, the subscript t refers to quantities relevant to the tangential kinematics with t_t^{stuck}, k_t, and u_t denoting the tangential stuck traction, traction-stiffness, and tangential relative displacement respectively. The hysteretic modification on this is done by introducing a "stick limit condition" using Coulomb's law and by rewriting the equation in the rate-form. The limit condition is usually taken as the magnitude of tangential forces not exceeding the normal traction scaled by the coefficient of friction (reminiscent of Coulomb's original law). Thus, the rate-dependent hysteretic modification of this is

$$\frac{dt_t}{ds} = \begin{cases} k_t \frac{du_t}{ds} + \frac{dk_t}{du_n}\frac{du_n}{ds} u_t & \text{stuck} \\ 0 & \text{slipped/separated}, \end{cases} \tag{17}$$

where s is some state-evolution variable (such as time) and u_n is used to denote the relative normal displacement. Using an explicit Euler scheme for integrating this between successive points, one can replace the rate-dependence to explicit (hysteretic) state dependence. This yields a functional form that is similar (but generalized) to previous path dependent friction implementations (such as the popular elastic dry friction/Jenkins element in [61]), and is represented as

$$t_t = \begin{cases} 0 & \text{separated} \\ k_t(u_t - u_{t0}) + \frac{dk_t}{du_n}(u_n - u_{n0})u_t + t_{t0} & \text{stuck} \\ t_t^0 & \text{slipped}. \end{cases} \tag{18}$$

The subscripts 0 are used to denote the historical quantities, or the quantities at the "previous" s-step. The "Coulomb cone" idea is used to obtain the post-slip behavior. Slippage is defined as the condition where the total magnitude of the planar tractions is equal to the stick limit. Since slippage cannot introduce rotational moments in the system, it is observed that the planar orientation of the traction vector is preserved across stick–slip state transitions. Consequently, a "stick-prediction" direction is obtained by norming the traction predicted for the stuck state in eq. (18) to give

$$\begin{Bmatrix} \widehat{t}_{sp}^x \\ \widehat{t}_{sp}^y \end{Bmatrix} = \frac{1}{\sqrt{\left(t_t^{x,stuck}\right)^2 + \left(t_t^{y,stuck}\right)^2}} \begin{Bmatrix} t_t^{x,stuck} \\ t_t^{y,stuck} \end{Bmatrix} = \frac{1}{||t_t^{stuck}||} \begin{Bmatrix} t_t^{x,stuck} \\ t_t^{y,stuck} \end{Bmatrix}. \tag{19}$$

This completes the formulation, allowing the tangential tractions to be expressed as

$$t_t^q = \begin{cases} 0 & t_n = 0 \ \text{(separation)} \\ k_t^q(u_t^q - u_{t0}^q) + \frac{dk_t^q}{du_n}(u_n - u_{n0})u_t^q + t_{t0}^q & ||t_t^{stuck}|| < \mu t_n \ \text{(stick)} \\ \mu t_n \widehat{t}_{sp}^q & \text{otherwise (slip)}. \end{cases} \tag{20}$$

The symbol q is used to denote either of the planar coordinates x, y and that the tangential laws for the two directions are identical in form. Classical marching-based stick–slip estimation techniques [61] could be followed for estimating the Jacobians for a Harmonic balance solver, while specifying appropriate "initial states" t_{t0} and u_{t0} will be sufficient for a quasi-static solver (see section 3.1.2 for the current implementation). These quantities are only updated at points of direction change in the hysteretic cycle since the response is taken to be monotonic between the direction reversal points. At the point of direction change, all frictional elements are instantaneously stuck, and this information is transmitted by saving the displacements and tractions and accounting for them in the following steps using the above path/history variables. However, in order to stay consistent with the fact that the normal contact is always in the elastic regime, the normal contact law is not implemented in this manner.

In studies such as [44,46], a relationship is established between the linearized stiffnesses in the normal and tangential directions in terms of a constant χ (taken to be 2.0 here) and the Poisson's ratio ν. There have been different studies formulating the exact form [16,21,44,46,62–66], and the current work, uses the tangential compliance estimate as in [44,46], which proposes the tangential force law per asperity as

$$\begin{aligned} T_t^q &= \tfrac{2\chi \cdot E}{(2-\nu)(1+\nu)}\beta_q \cdot d_q \\ &= \tfrac{4E}{(2-\nu)(1+\nu)}\beta_q \cdot d_q, \\ \text{where}, \beta_q &= \left(\tfrac{1}{R_1^q}+\tfrac{1}{R_2^q}\right)^{-1}. \end{aligned} \tag{21}$$

In the above, scripts q denote x or y components, β_q is the effective asperity radius from the two surfaces, and d_q is the imposed tangential relative displacement along the q component. As already noted, the orthotropy axes for the interface are assumed to coincide with the coordinate x, y axes. Carrying out the integrals and dividing by the region area A^e (as in eq. (14)), the elastic tangential traction is,

$$\begin{aligned} t_t^q &= u_t^q \tfrac{4E}{(2-\nu)(1+\nu)}\beta_t \mathbb{P}(z > \delta_n) \\ &= u_t^q \underbrace{\frac{4E}{(2-\nu)(1+\nu)}\beta_t \mathbb{P}\left(z > \left(z_p - d_n\right)\right)}_{k_t^q}. \end{aligned} \tag{22}$$

The tangential stiffness is thus only a function of the normal relative displacement, and is not an explicit function of the tangential relative displacement. Here the subscripts n are used for δ to emphasize the fact that it denotes the normal interference $z_p - d_n$. This is the only difference in formulation in comparison to [47], wherein the tangential stiffnesses were all assumed to be constant.

The statistic occurring above ($\mathbb{P}\left(z > \left(z_p - d_n\right)\right)$) is the complementary cumulative density function (ccdf) of z, which may be evaluated either using the exact integral

$$\mathbb{P}(z > \zeta) = \overline{F}_Z(\zeta) = \int_\zeta^\infty \phi(z)dz, \tag{23}$$

or with a finite sample empirical estimator using the count statistic

$$\widehat{\mathbb{P}}(z > \zeta) = \widehat{\overline{F}}_Z(\zeta) = \frac{1}{N_s}\sum_{i=1}^{N_s}\mathbf{1}_{Z_i>\zeta}. \tag{24}$$

Similar to the estimator for the expectation in Eq. (13), this may be evaluated for a finite sample and then fitted to an appropriate curve that may be used for the dynamical model.

2.3. Parametric interface characterization

For the traction model of section 2.2, the most relevant quantities that have to be determined from interfacial scans are the asperity peak heights and asperity radii along each direction. Additionally, "meso-scale" features must also be extracted so that flatness imperfections in the topology of the interface (such as from machining or warpage) can be accounted for.

First, a bi-linear plane (of the form $z = a_0 + a_1x + a_2y + a_3xy$) is fitted to the raw data to obtain the approximate underlying surface. This is then normalized with respect to the tallest point over the whole interface such that the tallest point becomes zero and the rest of the surface is a positive distance away. This normalization is carried out since it is assumed that prestress is the only mechanism through which asperities interact, and for zero prestress, no asperity is undergoing deformation. This reorients the raw data, so that it is in a convenient form to be incorporated into the contact model. A point is said to be separated from its counterpart on the other surface if the normal relative displacement at that point is lesser than the value of the above plane evaluated there. A sample of the raw data and its processed form for a single element are shown in Fig. 3a and b.

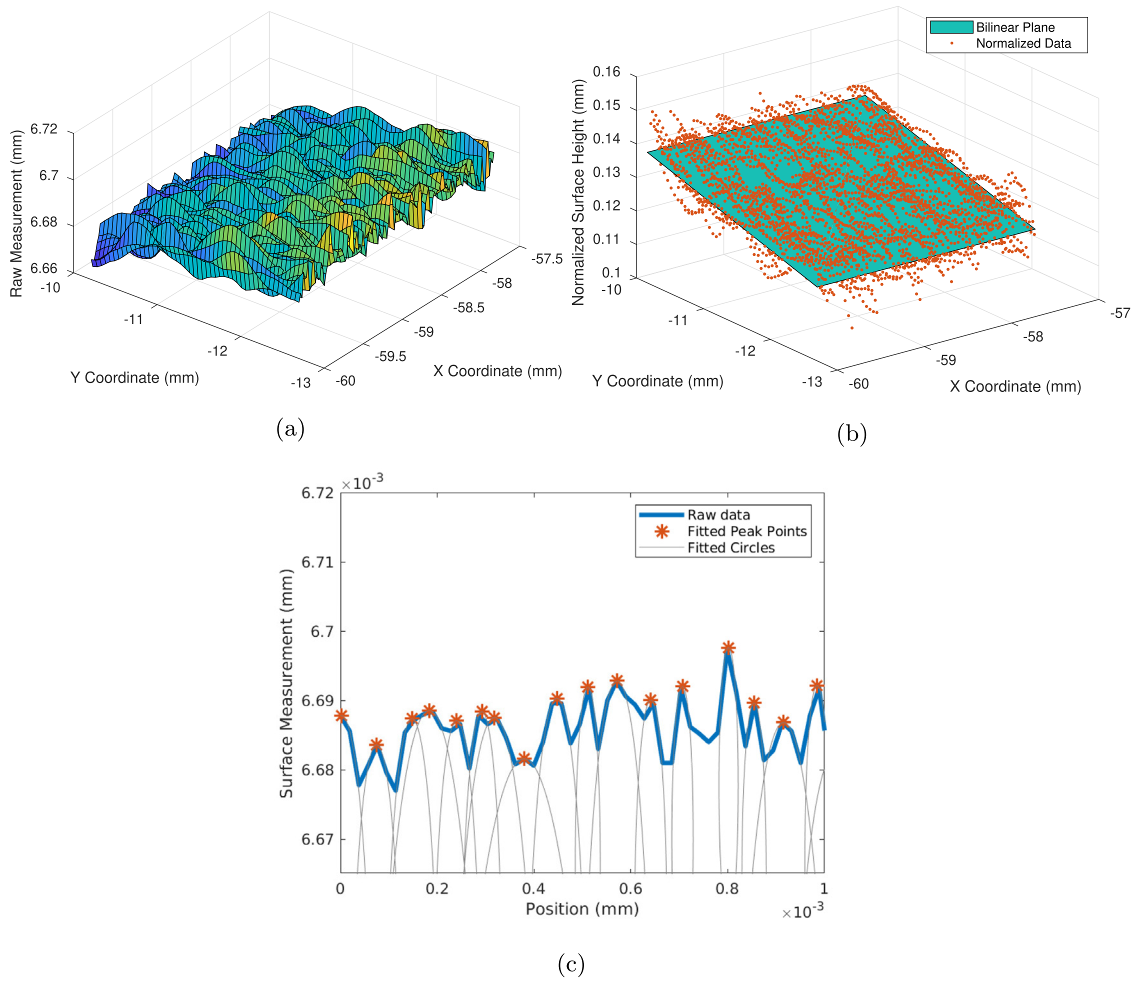

Fig. 3. Processing interfacial scan data: (a) a 3D view of raw data over a finite element; (b) Data upon surface bi-linear fitting; (c) kernel-interpolated fits of asperity peaks to circles.

Following this, the asperities, assumed to be manifested as local peaks in the raw data, are analyzed. In [67], the authors consider a few popular methods for numerically evaluating the relevant roughness parameters from a surface scan. Drawing inspiration from the three-point-peak (3PP) method, a kernel-integrated approach is followed here. Local kernels of three data points are fitted to a quadratic polynomial and analyzed using the coefficients if a peak exists within the kernel. After establishing conditionals to ensure that the same peak is not counted more than once, the kernel is moved across the data in each scan direction to obtain estimates of corresponding peak properties.

The local quadratic polynomials, expressed in the form $z = b_0 + b_1 x + b_2 x^2$ (with x being the position variable and b_i being the coefficients), allow the peak location, height and its circular radius to be estimated by,

$$\begin{aligned} x_{peak} &= -\frac{b_1}{2b_2} \\ z_{peak} &= b_0 - \frac{b_1^2}{4b_2} \\ R_{peak} &= -\frac{1}{2b_2}. \end{aligned} \tag{25}$$

Once this one-dimensional scan is conducted in each direction, peak heights and radii are obtained for the asperities as viewed along each scan direction. Fig. 3c depicts the results of a portion of a single line from a single element. It can be observed that the implementation identifies all of the peaks satisfactorily. A more accurate implementation might conduct this on the full 2D data, fitting ellipsoids from contours. That would allow for the detection of arbitrarily oriented orthotropy axes if they exist.

There are two challenges for the implementation of the traction in Eq. (14) and the traction-stiffness in Eq. (22). First, it is not always trivial to estimate the exact number of asperities in an interface since the "peaks" are more wavy than sharp (observe aspect ratios in Fig. 3c). Second, it will be very expensive to save complete non-parametric models of the interfacial asperities for each element in a mesh. Even if it is possible to accommodate such fidelity computationally, the storage overhead this will introduce is prohibitive. While addressing the former forms the rest of the current subsection, the latter will be dealt with in section 2.4.

For the first issue, an asperity-packing argument is made in order to obtain estimates of the number of asperities on a given element. Each asperity, on a two-dimensional snapshot, is idealized in Fig. 4a. Representing the radius, height and effective width with R, z, and w respectively, the relationship for the effective width, which is the projection of the asperity onto the plane of the interface, is

$$w = \sqrt{z(2R - z)}. \tag{26}$$

Since the radii are estimated for the two scanning directions as β_X and β_Y in the current study, the projection of each asperity is idealized to be an ellipse with axes $w_X = \sqrt{z(2\beta_X - z)}$ and $w_Y = \sqrt{z(2\beta_Y - z)}$. In order to get an estimate of the number of asperities within a region, it is hypothesized that each peak is adjacent to a valley and the geometry of the valleys are identical to that of the peaks. This results in a uniform square packing as in Fig. 4b, with packing efficiency 0.5.

Thus, the number of elements in a given region is estimated by the fraction of full ellipses that may be packed into the element area multiplied by the packing efficiency. This yields the estimate

$$\widehat{N} = \eta \frac{A^e}{\pi w_X w_Y}, \tag{27}$$

where η is used to denote the packing efficiency. Although there are ways of accounting for the gaps that will be present in the packing efficiency, this will have to be done on an element-by-element basis since the gap distribution on an arbitrary polygon is not trivial. Packing of ellipses in a generic triangle or a quadrilateral is by itself a fairly challenging problem, but setting $\eta = 0.5$ is assumed to be nominally valid for the current work. The interested reader is directed to [68,69] and similar works for more details.

2.4. Parametric interface response characterization

Coming to the second issue (from the previous subsection) related to the accurate evaluation of the statistics (the integral expressions), previous works such as [21,22,58] developed results making specific assumptions about the distribution function $\phi(z)$ (such as positing it to be an exponential distribution). In the current study however, the local contact response is simulated by evaluating the estimators in Eqs. (13) and (24) using bootstrapped peak heights from the region of interest, followed by fitting the response with an appropriate function. There have been several earlier studies following a similar idea, such as [60], where an exponential function and a smoothened hysteretic model are fitted to the normal and tangential traction laws respectively, and [25] where nonlinear piece-wise power law relationships are employed for both laws.

The colored lines in Fig. 5 show the empirically determined normal traction and x-direction tangential traction-stiffness as the normal displacement is varied for a single element in the interface (note that the normal displacement denotes the global interference of the two surfaces, with negative values corresponding to contact separation). The first large kink in each curve denotes the height of the second asperity, i.e., before that, only a single asperity was in contact. The 95% confidence intervals for the characteristics calculated using 30 bootstrapped samples are depicted for each case (see colored-dashed lines), from which it is apparent that the maximal uncertainty is in the low displacement regime where the number of engaged asperities is low.

Inspecting the shape of the curves, smooth functions are fitted to the data to aid the implementation. For the normal traction, a power law with a "Gaussian dip" term is used, giving the form,

$$\log t_n = a + b \log u_n + c \exp\left(-\frac{1}{2}\left(\frac{\log u_n + d}{e}\right)^2\right), \tag{28}$$

with a, b, c, d, e being the fitting parameters. For the tangential traction-stiffness, a hyperbolic tangent function is employed to fit the smoothed step-like behavior of the ccdf. This is expressed as,

$$\log k_t = a + b \tanh\left(d(\log u_n - c)\right). \tag{29}$$

Here, a, b, c, d are fitting parameters (different from the ones used in Eq. (28)). It must be noted that simplifications of the former with a simple power law and the latter with a piece-wise constant function were avoided since the operational regime of the models are around the region where the trends seem to show the dips and transitions respectively. The fits for the reference element may be observed in Fig. 5 as black lines with dash patterns.

Once these fits are conducted for the asperities in each element of an interface, the parameters may be transmitted across for system-level simulations. Now that the models are established, the only unknown that will have to be determined is the coefficient of friction μ. Although there are studies that estimate μ from rough contact parameters (such as the ones used in

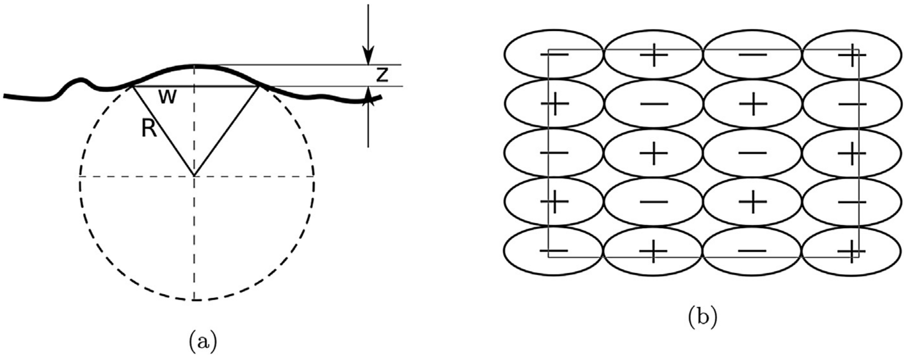

Fig. 4. (a) 2D geometry and (b) Spatial distribution of asperities in the interface.

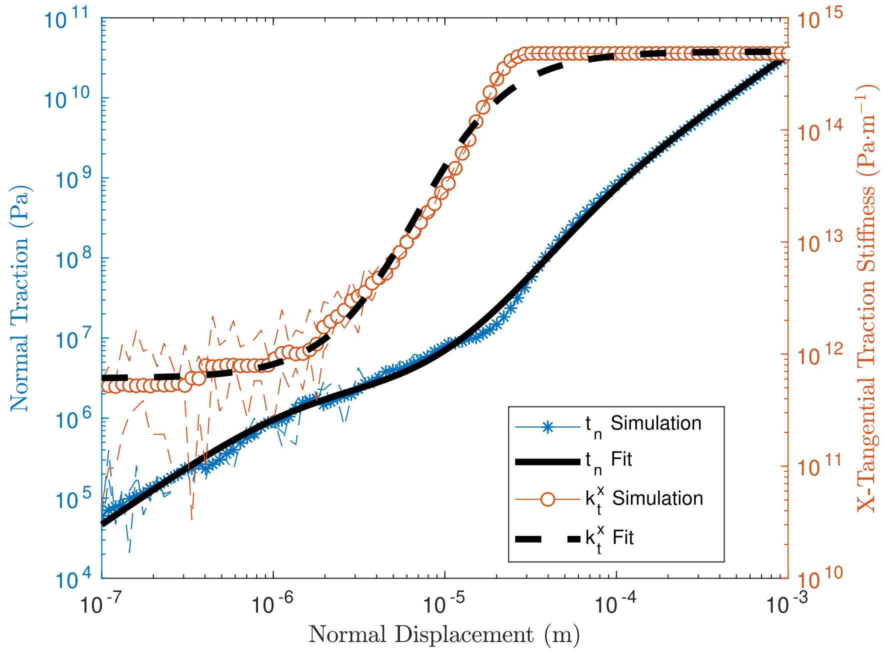

Fig. 5. Statistical response characterization and fits. The left and right vertical axes are used for t_n and k_t^x respectively. The 95% bootstrap confidence limits are highlighted using dashed lines for each case.

[25]), these are not used in the current formulation and the value is thought to be a constant lying somewhere between 0 and 1 (from physical arguments pertaining to dry friction). The influence of μ is studied parametrically for the chosen application case.

In summary, it must be noted that the current constitutive modeling approach has the advantages that it:

- Is multi-scale in the sense of relating macro-level responses (tractions, stiffnesses) using meso- and micro-level features;
- Is capable of approximating the rough contact response without too much overhead for a macro-level simulation;
- Is capable of accounting for localized variations across different parts of a surface;
- Enables the study of the evolution of relevant roughness properties with experimentation and their correlations with the system-level responses.

3. Benchmark application

The current section applies the developed modeling framework for a bolted joint benchmark. The different processes are summarized as a flowchart in Fig. 6. As can be seen, the modeling approach is coupled with surface assessments of the interfaces in the system. The non-linear analysis is conducted using the contact model developed through surface scan data

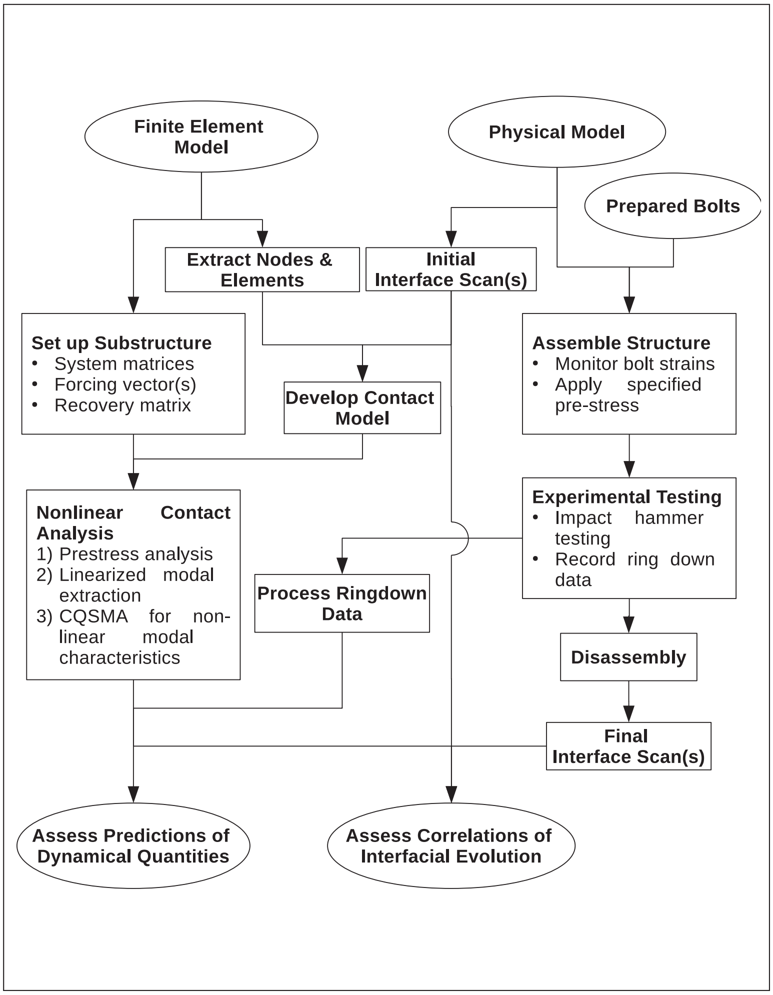

Fig. 6. Summary of application framework.

imposed on the finite element mesh. Since such scans are non-destructive, practical deployment of the framework will not incur any significant overhead in resource requirements beyond the need for specimens to be fabricated.

Following the interfacial scan, dynamic experiments are conducted in order to assess the model results. Since a quasi-static modal approach is used for the simulations, experimental ring down data from impact hammer tests are transformed into modal backbones for comparison. Following this, in order to study how features on the interface change during the dynamical tests, interfacial scans are conducted after disassembly. The differences in the parameters are used for testing correlations with simulated interfacial field quantities.

3.1. The Brake-Reuß beam: a bolted assembly

The Brake-Reuß Beam (BRB) is a bolted assembly structure [49] that consists of two "half-beams" connected together using a lap-joint realized using three bolts. Depicted in Fig. 7a, the total length of the assembly is approximately 720 mm (28.375 inches) and has a 1 in$\times$1 in square cross-section. Joining the beams, three sets of 5/16 bolts, nuts and washers are used. The total length of the interface is 120 mm, with the holes separated by 30 mm center-to-center on both half-beams. Fig. 7a depicts an ABAQUS model of the beam. Each bolt is pre-stressed equally.

The beam is meshed in such a way that it has a 10×10 grid of cubic (quad, C3D8R) elements in the square cross-section, and the holes are meshed with 32 quad elements to have a reasonably sized mesh for dynamic analysis. The mesh is shown in Fig. 7b.

The assembly is set up by creating CAD models of the "half-beams", bolts, nuts and washers, and assembling them in ABAQUS. Mesh tie constraints are specified between the bolt-washer, washer-half beam, and nuts-washer interface. Note that no constraint is specified between the interfaces and/or the bolts and nuts at this stage.

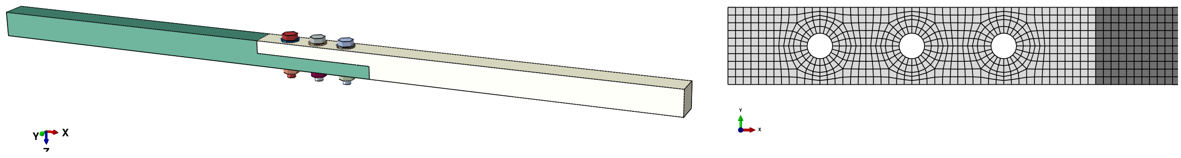

(a) (b)

Fig. 7. The Brake-Reuß Beam Benchmark: (a) Assembly; (b) Interfacial Mesh.

3.1.1. Assembly modeling

In order to have a physically appropriate means of applying the prestress that can be used in substructured analyses, it becomes necessary to model the interaction between the bolts and nuts in a reasonably accurate fashion. The idea followed here is to arrest any relative motion in the plane perpendicular to the axis of the bolt (preventing any interpenetration) and allow free translation along it. In order to realize this, virtual nodes are introduced and coupled to the inner and outer contact surfaces of the nuts and the bolts respectively (see Fig. 8), and the planar degrees of freedom (x, y in this case) are constrained to be equal for the two nodes using Multi-Point Constraints.

The actual prestress is realized by having appropriately directed nodal forces at these virtual nodes, i.e., a compressive force along the $-\hat{z}$ direction is applied on the nut-coupling nodes and a tensile load along the $+\hat{z}$ direction is applied on the bolt-coupling nodes, all with magnitudes specified by the prestress level.

It must be noted that the above assembly, in the unstressed state, has seven eigenvalues corresponding to rigid body modes (the degeneracy of the non-straining zero-energy modes is seven), with six components coming from the full assembly lacking any boundaries and the seventh arising out of the fact that translation along the bolt axis is not constrained. However, once the loads are applied in the presence of an interfacial model, the degeneracy will reduce to 6, corresponding to the rigid body modes of the assembled system.

In most solution approaches involving zero-energy modes (ZEMs), the ZEMs are first constrained out by estimating their null-space and projecting the system onto it. For interfacial modeling applications with assemblies similar to the above, however, not all of the ZEMs may be constrained out since the one with the translation along the bolt axis has a non-trivial contribution to the response of the system. It thus becomes necessary to identify the correct set of six ZEMs to constrain out. This is carried out here by first transforming the system to a relative coordinate representation and then identifying the "stuck interface" ZEMs that impart no straining of the interface. Denoting the degrees of freedom of the top and bottom interfaces and the rest of the degrees of freedom as $\tilde{u_T}, \tilde{u_B}$ and $\tilde{u_R}$ respectively, the relative coordinate transformation is achieved as follows:

$$\begin{Bmatrix} \tilde{u_T} \\ \tilde{u_B} \\ \tilde{u_R} \end{Bmatrix} = \underbrace{\begin{bmatrix} \boldsymbol{I} & \boldsymbol{I} & \boldsymbol{0} \\ \boldsymbol{0} & \boldsymbol{I} & \boldsymbol{0} \\ \boldsymbol{0} & \boldsymbol{0} & \boldsymbol{I} \end{bmatrix}}_{\mathcal{T}_{\mathcal{R}}} \begin{Bmatrix} \Delta\tilde{u} \\ \tilde{u_B} \\ \tilde{u_R} \end{Bmatrix}. \tag{30}$$

Here, $\Delta\tilde{u} = \tilde{u_T} - \tilde{u_B}$, is the relative displacement across the interface. This is followed by a Galerkin projection using the same matrix to transform the original system to the relative coordinate representation. From this representation, the fully stuck ZEMs may be estimated as the eigenvectors of the system formed by excluding the rows and columns corresponding to the relative DOFs (setting $\Delta\tilde{u}$ to zero). From physical arguments, it can be seen that the degeneracy of ZEM is just six for the stuck interface system (and this can be verified numerically). These modes may now be transformed back to the original relative coordinate representation by prepending it with an appropriate number of zeros. Stacked as columns, this set of six modes forms the ZEM matrix $\boldsymbol{\mathcal{Z}}$ whose null-space basis vectors $\boldsymbol{\mathcal{L}}$ (subject to a mass-weighted inner product) is then used to transform the system to be expressed in terms of the null-reduced DOFs $\tilde{u_n}$. This may be expressed as,

$$\begin{Bmatrix} \Delta\tilde{u} \\ \tilde{u_B} \\ \tilde{u_R} \end{Bmatrix} = [\boldsymbol{\mathcal{L}}] \begin{Bmatrix} \tilde{u_n} \end{Bmatrix}. \tag{31}$$

The final system inertia matrix $\boldsymbol{M}$, stiffness matrix $\boldsymbol{K}$, and bolt load vector $\tilde{F_b}$ are given, after the above two transformations, in terms of their original counterparts (characterized with $\widehat{\cdot}$s) as

$$\begin{aligned} \boldsymbol{M} &= \mathcal{L}^T \mathcal{T}_{\mathcal{R}}^T \widehat{\boldsymbol{M}} \mathcal{T}_{\mathcal{R}} \mathcal{L} \\ \boldsymbol{K} &= \mathcal{L}^T \mathcal{T}_{\mathcal{R}}^T \widehat{\boldsymbol{K}} \mathcal{T}_{\mathcal{R}} \mathcal{L} \\ \tilde{F_b} &= \mathcal{L}^T \mathcal{T}_{\mathcal{R}}^T \widehat{\tilde{F_b}}. \end{aligned} \tag{32}$$

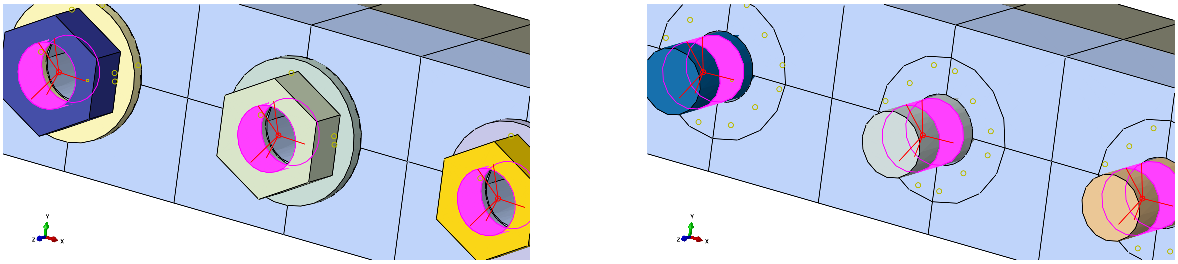

(a) (b)

Fig. 8. Coupling constraints used for the assembly: (a) Inner surface of nut coupled to a virtual point; (b) Outer surface of bolt coupled to a virtual point.

The linear system comprising of $\boldsymbol{M}$ and $\boldsymbol{K}$ has a single ZEM corresponding to the translation along the bolt axis that has not been constrained out in eq. (31). Thus, the system is ill-posed in the absence of a contact model and has to be studied only in the presence of a model for the interface.

In practice, all of the steps from eq. (30) are carried out on substructures constructed using fixed interface component modes extracted from the Finite Element program (ABAQUS).

3.1.2. Nonlinear modeling

For the nonlinear modeling, the contact models developed in section 2.2 are applied with the ZTE's (section 2.1) from the relative coordinate system and then transformed to the null-reduced system through $\boldsymbol{\mathcal{L}}$. For a general excitation force $\tilde{F}^{ex}(t)$ expressed in relative coordinates, the nonlinear dynamic system is

$$\boldsymbol{M}\ddot{\tilde{u}}_n + \boldsymbol{K}\tilde{u}_n + \boldsymbol{\mathcal{L}}^T\tilde{F}_{nl}(\boldsymbol{\mathcal{L}}\tilde{u}_n, \dots) = \tilde{F}_b + \boldsymbol{\mathcal{L}}^T\tilde{F}^{ex}(t). \tag{33}$$

For static analysis, say of just the bolt prestress, the dynamic terms are dropped and the problem is solved quasi-statically.

For dynamic calculations, an improved nonlinear hysteretic implementation of the Quasi-Static Modal Analysis (QSMA) approach expounded in [15] is formulated. The difference between the current Coupled Quasi-Static Modal Analysis (CQSMA) approach and the previous approach is twofold: (a) QSMA decouples the static and dynamic simulation steps, while CQSMA conducts the simulations in a coupled manner and conducts the decoupling only in the analysis/post-processing part; and (b) CQSMA is generalized for non-Masing models too, while QSMA has only been used with Masing's hypothesis so far.

For QSMA [15], the static pressure distribution is incorporated into the dynamic analysis by conducting all of the analyses on a perturbation of the solution from this step. Denoting the solution of the static problem by $\tilde{u}^*$ and the perturbed solution by $\tilde{u} = \tilde{u}^* + \tilde{\delta}^u$ (with $\tilde{\delta}^u$ being the perturbation), it is shown that the equations of motion can be reduced, using a first order Taylor's expansion about the static solution, to

$$\begin{aligned} \boldsymbol{M}\ddot{\underset{\sim}{u}} + \boldsymbol{K}\underset{\sim}{u} + \underset{\sim}{F}^{nc}(\underset{\sim}{u}) + \underset{\sim}{F}^{frict}(\underset{\sim}{u}) &= \underset{\sim}{F}^{bolt} + \underset{\sim}{F}^{ext}(t) \\ \boldsymbol{M}\ddot{\underset{\sim}{\delta}}^u + \underbrace{\boldsymbol{K}(\underset{\sim}{u}^* + \underset{\sim}{\delta}^u) + \underset{\sim}{F}^{nc}(\underset{\sim}{u}^*) + \left.\frac{\partial \underset{\sim}{F}^{nc}}{\partial \underset{\sim}{u}}\right|_{\underset{\sim}{u}^*}\underset{\sim}{\delta}^u}_{\text{Taylor's Expansion}} + \underset{\sim}{F}^{frict}(\underset{\sim}{u}) &= \underset{\sim}{F}^{bolt} + \underset{\sim}{F}^{ext}(t) \\ \implies \boldsymbol{M}\ddot{\underset{\sim}{\delta}}^u + \underbrace{\left(\boldsymbol{K} + \frac{\partial \underset{\sim}{F}^{nc}}{\partial \underset{\sim}{u}}\right)}_{\boldsymbol{K}^A}\underset{\sim}{\delta}^u + \underset{\sim}{F}^{frict}(\underset{\sim}{u}) &= \underset{\sim}{F}^{ext}(t). \end{aligned} \tag{34}$$

Here, the forcing vectors $\tilde{F}^{nc}, \tilde{F}^{frict}, \tilde{F}^{bolt}$, and $\tilde{F}^{ext}$ denote the normal contact forcing used for the static analysis, the frictional contact model used for the dynamic analysis, the constant bolt load, and the external excitation respectively. The main drawback here is that it is not appropriate to use a nonlinear normal contact model for the dynamic analysis since it has already been linearized into the Jacobian, and doing so will introduce an over-stiffening effect on the interface.

Following this, the modal characteristics are extracted by applying a quasi-static forcing in the shape of the corresponding mode shape, ϕ, of this augmented system. The nonlinear problem becomes

$$\boldsymbol{K_A}\tilde{\delta}^u + \tilde{F}^{frict}(\tilde{u}) = \alpha\boldsymbol{M}\tilde{\phi}, \tag{35}$$

where α is the modal forcing amplitude. The natural frequency at a particular forcing amplitude α is given by the secant stiffness of the modal hysteresis loop and the damping factor is given using the area inside the hysteresis loop. The exact expressions commonly encountered are

$$q = \tilde{\phi}^T \boldsymbol{M} \tilde{\delta}^u; \qquad \omega = \sqrt{\frac{\alpha}{q}}; \qquad \zeta = \frac{D}{2\pi(q\omega)^2}. \tag{36}$$

The dissipation is sometimes more accurately estimated by calculating it individually for each frictional element in the model and summing them up.

Taking inspiration from the above, CQSMA starts off by first solving the prestress problem

$$\boldsymbol{K}\tilde{u}^* + \tilde{F_{nl}}(\tilde{u}^*) = \tilde{F}^{bolt}, \tag{37}$$

after which the mode shape, $\tilde{\phi}$, is calculated about the Jacobian evaluated at the solution $\tilde{u}^*$ (similar to QSMA). For the dynamic analysis, the full system, given by

$$\boldsymbol{M}\ddot{\tilde{u}} + \boldsymbol{K}\tilde{u} + \tilde{F_{nl}}(\tilde{u}) = \tilde{F}^{bolt} + \tilde{F}^{ext}(t), \tag{38}$$

is used instead of the perturbation. Note that there is no need to separate the normal and frictional contact models here. However, the modal forcing vector is constructed based on the mode-shapes of the augmented system linearized about the prestress solution as before,

$$\left[\left(\boldsymbol{K} + \frac{\partial \tilde{F_{nl}}}{\partial \tilde{u}}\right) - \omega^2 \boldsymbol{M}\right]\tilde{\phi} = \tilde{0}. \tag{39}$$

This sets up the following system for the modal quasi-static analysis:

$$\boldsymbol{K}\tilde{u} + \tilde{F_{nl}}(\tilde{u}) = \tilde{F}^{bolt} + \alpha \boldsymbol{M}\tilde{\phi}. \tag{40}$$

The modal amplitude here is determined by taking the inner product of the deviation of the CQSMA solution $\tilde{u}$ from the static solution $\tilde{u}^*$ with the chosen linearized mode shape as

$$q = \tilde{\phi}^T \boldsymbol{M}(\tilde{u} - \tilde{u}^*). \tag{41}$$

In a like manner, the dissipation is taken as the work done by the perturbation tractions on the perturbation displacement field in the interface. Thus, the modal characteristics are estimated by,

$$\omega = \sqrt{\frac{\alpha}{q}}; \qquad \zeta = \frac{D(\tilde{u} - \tilde{u}^*, \tilde{t} - \tilde{t}^*)}{2\pi(q\omega)^2}. \tag{42}$$

$\tilde{t}^*$ has been used here to denote the tractions at the end of the static analysis. These are subtracted from the traction vector since the work done by the tractions developed in the pre-stress step is not of any significance for dynamic operation. The history-dependent manner in which the contact models are formulated in section 2.2 naturally lends them to hysteretic quasi-static calculations, thus generalizing the approach to non-Masing problems (such as those with separation). In the current work, the hysteresis loop is idealized as a polygon with a prescribed number of vertices and the area within it is calculated using the Surveyor's/shoelace formula [70]. For a planar polygon defined by vertices (x_i, y_i), with $i = 1, \ldots, n$ ordered along clockwise, the formula for the area is given by the expression

$$A = \frac{1}{2}\left|\sum_{i=1}^{n-1} x_i y_{i+1} + x_n y_1 - \sum_{i=1}^{n-1} x_{i+1} y_i - x_1 y_n\right|. \tag{43}$$

If one estimates the hysteretic areas under the traction-displacement characteristics at any point on the interface, the derived quantity will be the flux of dissipation, i.e., the amount of energy dissipated per unit area at that location. Visualizing the flux of dissipation over the interface and classifying different portions of the interface based on it can be a very useful approach for wear and damage assessment and/or prediction. This will be used in section 4.3 for studying correlations to evolutionary trends.

Fig. 9 provides a detailed overview of the modeling approach. The different blocks summarize the different modeling and analysis steps followed in sections 3.1 to 3.3. Recall Fig. 6 for the context of this in the complete framework.

3.2. Experimental setup for interfacial scans

A Keyence in-line profilometer is used in the current study to scan the interfacial surfaces of the jointed connection. The profilometer measures the heights of points on a surface in a certain range (specifically −23 to 23 mm, where the 0 level corresponds to the point 80 mm vertically below the head) through a laser transmitter–receiver pair. As shown in Fig. 10a, the laser probe line sweeps through at a constant velocity (approximately 0.2 mm·s^{-1}) to extract the heights across the surface.

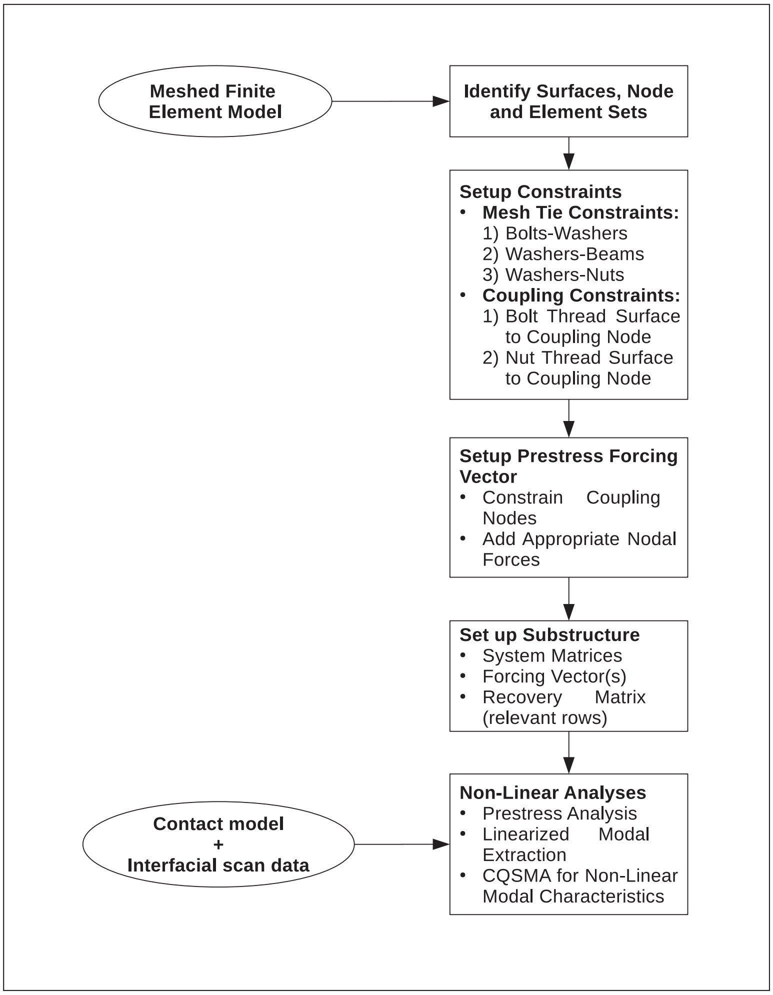

Fig. 9. Overview of Modeling approach.

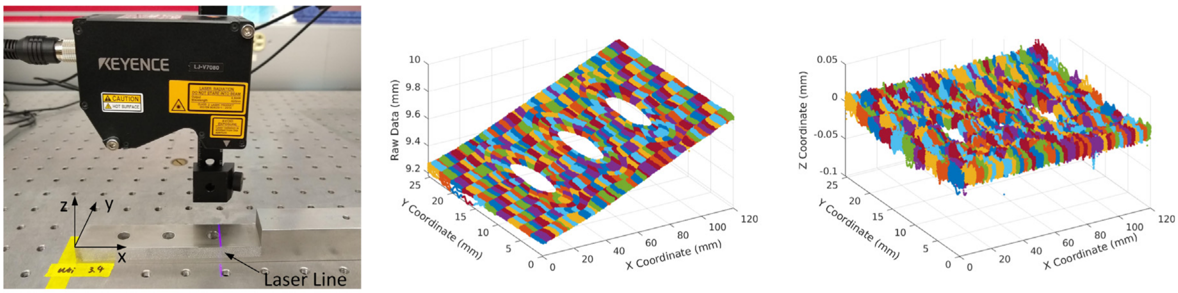

(a) (b) (c)

Fig. 10. Interface scanning setup: (a) The optical profilometer; (b) Raw data, and (b) Plane-adjusted data. (Colouring indicates element).

The vertical axis resolution of the instrument is approximately 0.5 μm and the x and y direction step sizes are (approximately) 30 µm and 50 µm respectively (coordinate systems as depicted in Fig. 10a). Although a much higher resolution device will be necessary for a more exact tribological characterization, this configuration was deemed sufficient for the current exploration.

In order to account for variations in the straightness of the beam and/or misalignment between the sweep direction and the surface tangential plane, it is first assumed that the interface itself is nominally flat and any variation seen in the extracted data is due to physical deviations of the beam from the ideal geometry. The raw data is de-trended by subtracting a trend plane that is built using the data along each free edge. Fig. 10b to c depict the raw and de-trended data for one such scan.

Following the procedures outlined in section 2.3, the relevant properties are estimated for each element in the interface after first localizing the data within the underlying finite element mesh. The element-wise total roughness parameter R_t is used as the peak heights in the current study (so that the asperity heights are all positive). The results from the scan are provided in Fig. 11. After this, the contact model parameters (five for normal traction and four each for the two tangential stiffnesses) are estimated by conducting the curve fits upon bootstrapped simulations for each element as outlined in section 2.4.

For constructing the interfacial meso-scale gaps fitted using the bilinear planes (see Fig. 11a), the planes are first fitted separately for both of the interfaces and then added together to estimate the "gap plane" that is useful for the analysis. This addition is justified by the assumption that the two interfaces do not interact when they are not pre-stressed (meaning that the gap function can never be negative). Following this, the contact condition at any location $\tilde{x} \in \Gamma$ (using Γ to denote the interface) becomes

$$u^n_{top}(\tilde{x}) - u^n_{bot}(\tilde{x}) \geqslant g_f(\tilde{x}), \tag{44}$$

where $g_f(\tilde{x})$ denotes the gap function and *top* and *bot* denote corresponding values from the top and bottom faces respectively. Since bi-linear planes are used for this, the function may easily be represented as the shape function-weighted sum of nodal contributions. In practice, the form $a_0 + a_1x + a_2y + a_3xy$, upon being fitted, is evaluated at four quadrature locations in each element and nodal values are extracted as the best possible values for representing the gap at the quadrature locations across all the elements in a least-squares sense (see Super-Convergent Points (SCP) in classical finite element texts such as [71]). Practically however, this was observed to be prone to experimental errors in the current experimental setup. This is due to the fact that no precise mechanism has been employed to ensure the co-planarity of the probe direction and the surface plane. Since the meso-scale interface is unreliable, simulations are conducted both with and without taking it into account in order to observe its influence on the response.

For the other parameters ($R_t, \beta_X, \beta_Y, \widehat{N}$), the interface values are taken as the average of the estimates for each of the faces. The estimates for these parameters, as opposed to the gap function, were found to be fairly repeatable across multiple scans and thus there is considerable confidence in the developed contact model parameters.

3.2.1. Adhesive effects

As remarked earlier, the influence of adhesion is assumed to be negligible in the current modeling approach. In order to assess this, the dimensionless intermolecular distance parameter that is used in [72,73] is computed. A key quantity required for this is the critical interference parameter

$$\omega_C = \left(\frac{\pi K H}{2E^*}\right)^2 R. \tag{45}$$

Here the effective radius R is taken as $\sqrt{\beta_X \beta_Y}$; the hardness H is taken as 9.47 GPa (from experimental data published in Ref. [74] for 2.2 mm radii spheres); the parameter K is taken as $0.454 + 0.41\nu$ (with $\nu = 0.29$ being Poisson's ratio, giving $K = 0.5729$); and the effective Young's modulus E^* taken as $E/(2(1-\nu^2))$ (E = 192.85 GPa, yielding E^* = 105.28 GPa). Using a typical inter molecular separation [72] of ϵ=0.4 nm, the dimensionless parameter ϵ/ω_C comes out to be less that 0.1% for all the elements (see histogram in Fig. 12a).

Furthermore, the relationship in Ref. [72] and the asperity geometries in section 2.3, may be used to estimate the expected adhesive traction. Fixing the work of adhesion value to 2.5 J/m^2 (data for low carbon steel on low carbon steel contact [75]), Fig. 12b plots the expected adhesive traction along with the fit established before for the elastic traction as functions of the normal displacement (global interference/relative displacement of the two interfaces). Note that the adhesive tractions, in keeping with the spirit of the presented approach, represent the average adhesive traction over the considered element and not the traction on any single asperity. It can be seen that there exists a threshold below which adhesive effects may not be ignored. However, since the operating regime for the current investigation (in the central region of the interface) involves normal displacements on the order of a micron or more, adhesive tractions are more than one order of magnitude lesser than elastic tractions. Studying the influence of adhesion in the outer regions of the interface on the dynamics of the system is beyond the scope of the current paper. The currently developed model therefore does not account for adhesive effects.

3.3. Experimental setup for static pre-stress

As mentioned earlier, there is a high amount of variability in the torque-tension relationship of bolts. The origins of these may range from material/geometric imperfections to environmental conditions and thus may not always be amenable to accurate modeling. Therefore, the current study utilizes an experimental technique developed in [5] to ensure better accuracy in the interfacial loading conditions. The threads in the bolts are machined off in the internal regions of the beam and strain gauges are attached to the curved surface of the bolt (see Fig. 13a).

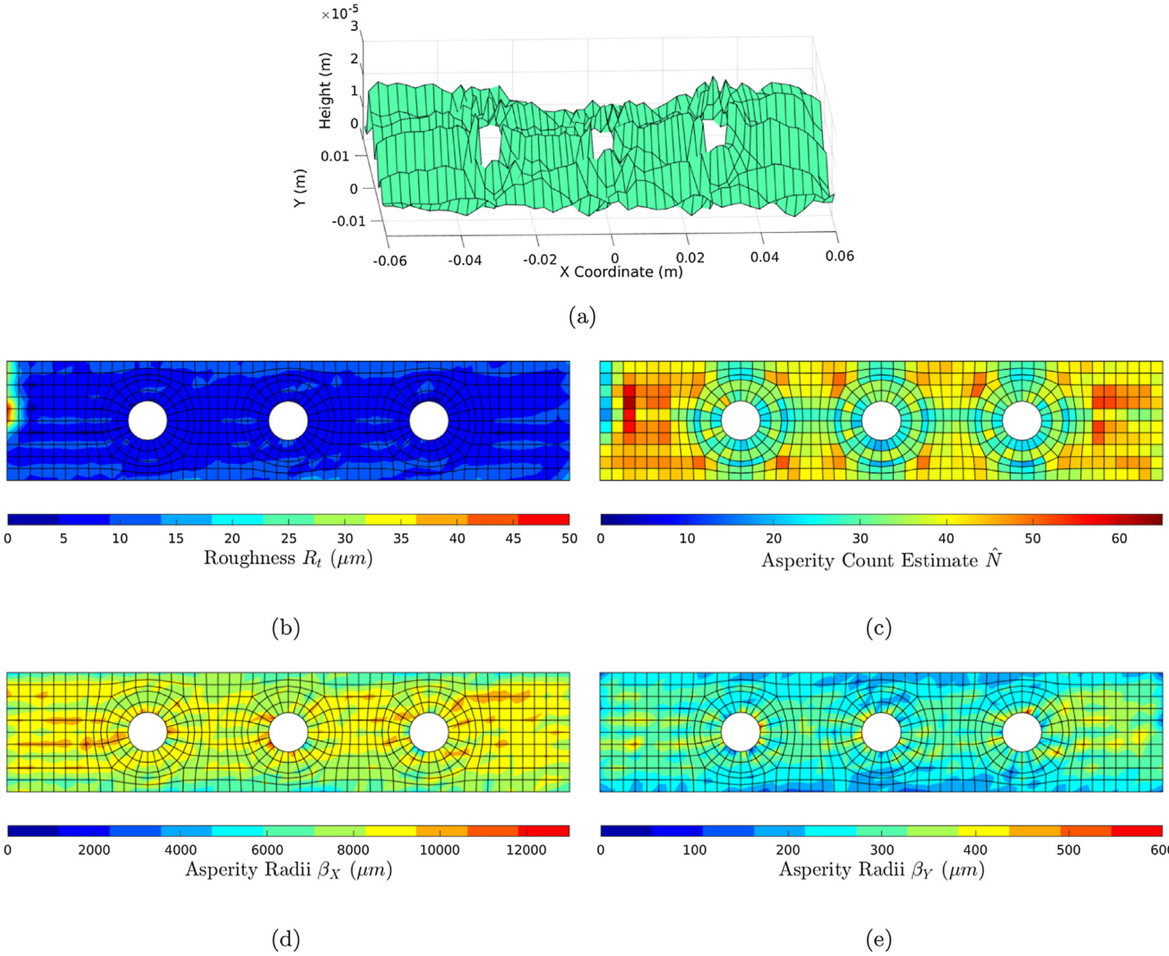

Fig. 11. Results of surface scan: (a) Interface fitted with bi-linear planar elements; (b) Surface roughness R_t; (c) Asperity count estimate per element $\widehat{N}$; (d) Radii when seen along horizontal (scan along vertical); and (e) Radii when seen along vertical (scan along horizontal).

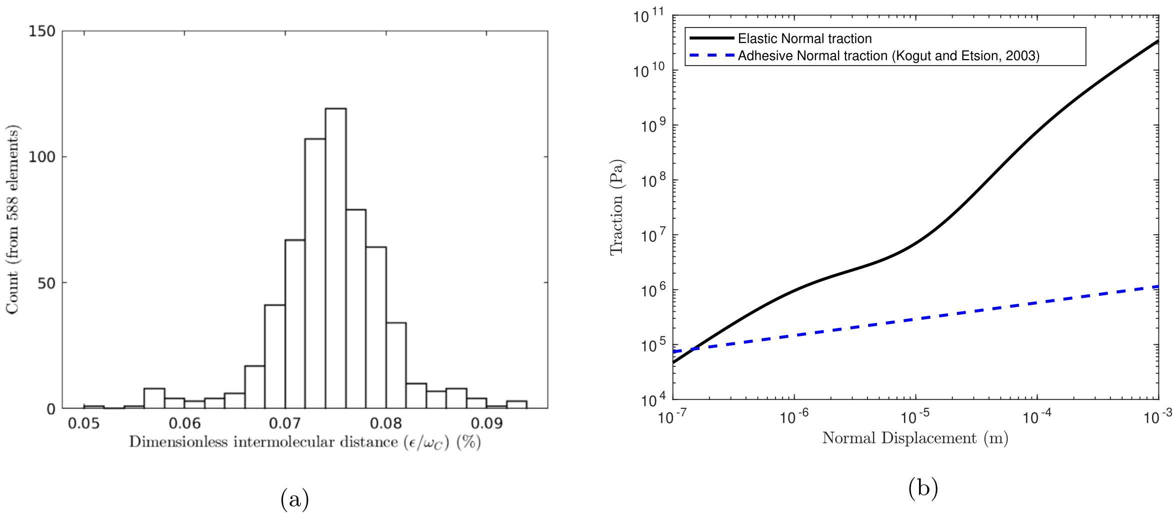

Fig. 12. Assessing influence of adhesion: (a) histogram of dimensionless intermolecular distance across all elements; and (b) comparison of elastic and adhesive normal traction for the indicative element (previously used in Fig. 5).

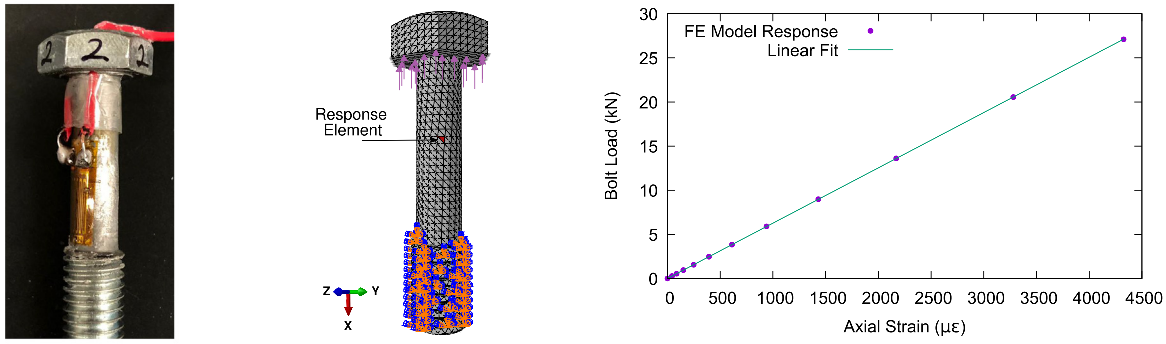

(a) (b) (c)

Fig. 13. Bolt pre-stress characterization (a) Experimental bolt with the strain gauge, (b) Finite element model with loading conditions and output element, and (c) Force-micro-strain response characteristics.

A finite element model of the modified bolt is prepared to characterize the force-strain characteristics. Since the deflections are expected to be in the linear domain, a linear finite element model is sufficient to capture the load–strain relationship (see Fig. 13b for the mesh and loading conditions). The model is fixed at the threads and loaded uniformly in the base surface of the bolt-head. The average strain from an element in the outer surface of the bolt (highlighted in red) is extracted for the study. The force-strain characteristic is fit to a linear function (see Fig. 13c) yielding the relationship

$$F = 6.2683 \times 10^6 \epsilon. \tag{46}$$

Here, F denotes the bolt load in N and ϵ, the strain. For the required load of 11.580 kN (corresponding to a 20 Nm preload (as per the analytical solution in [76]), the bolt must develop a strain of 1847 $\mu\epsilon$. However, experimentally the bolts were tightened to strains averaging around 2050 $\mu\epsilon$, which corresponds to a prestress level of 12.845 kN (using the same expression, corresponding to around a 20 Nm torque level). Thence, this prestress level was used in all the simulations

3.4. Experimental setup for dynamic testing

Fig. 14 depicts the test setup used for the impact hammer tests. The beam, after being assembled (with the prepared bolts) with the correct prestress levels, is suspended using two bungee cables. Two accelerometers are attached at the extreme ends and hammer impacts are made from the point shown in the figure. Five "medium level" impacts (~350 N amplitude), one "low level" (~80 N) and one "high level" impact (~850 N) are carried out on the current structure. The ring down acceleration data is recorded from the accelerometers in order to identify the nonlinear dynamic properties. The wires from the bolts were wrapped loosely around the assembly during the test. This configuration was determined, through multiple experiments, to have no appreciable effect on the dynamics of the system.

The current study focuses solely on responses dominated by the first bending mode in the system (depicted for a low amplitude case in Fig. 15). Thence, the data from one of the accelerometers is filtered around this frequency by a 4^{th}-order Butterworth bandpass filter and the Peak-Finding and Fitting (PFF) method (see [42]) is used to process the filtered data to obtain amplitude-modal characteristics of the system. This extracts the modal frequency and damping ratio as functions of the filtered amplitudes at the chosen accelerometer location. Since QSMA and CQSMA (Section 3.1.2) characterize the system when they are excited solely by the mode of interest, the corresponding amplitudes from the simulations may directly be correlated with the filtered amplitudes. In the current study, instead of retaining the end nodes as part of the boundary DOFs, the corresponding part of the recovery matrix (transforming subtructure DOFs to the FE model DOFs) is employed to extract the necessary amplitude since this is thought to provide a more accurate substructure than the former approach.

4. Results

4.1. Experimental Identification

In order to first identify the density and Young's modulus of the beam, low amplitude hammer tests are conducted for the half beams separately after having them weighed. The extracted values for density and Young's modulus are 7857.8 kg·m^{-3} and 192.85 GPa respectively.

Following this, the beams are tightened to a prestress of 12.845 kN (as mentioned before) by monitoring the strain experienced by the bolts and the nonlinear impact hammer tests are carried out following the procedure described in [77].

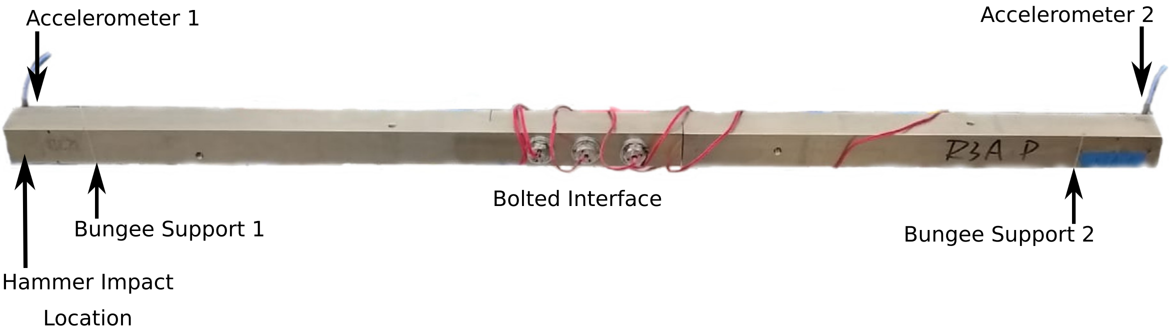

Fig. 14. Experimental Setup for Hammer Test.

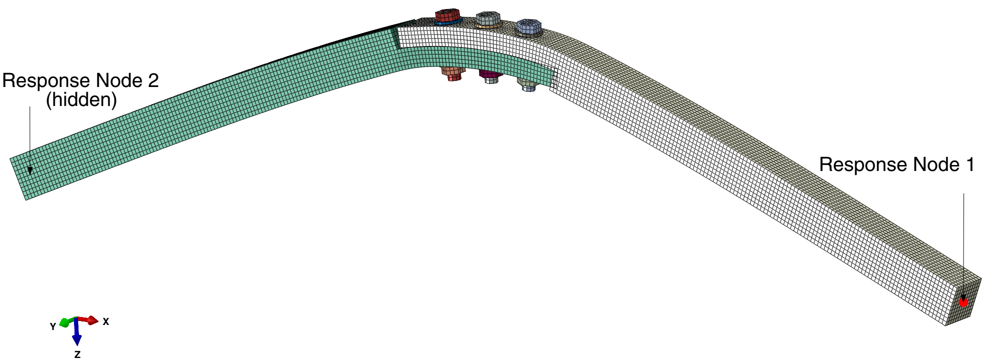

Fig. 15. The mode shape of interest: First bending mode (linearized about an Abaqus frictionless hard contact prestress simulation in Abaqus). The recovery nodes are highlighted in red.

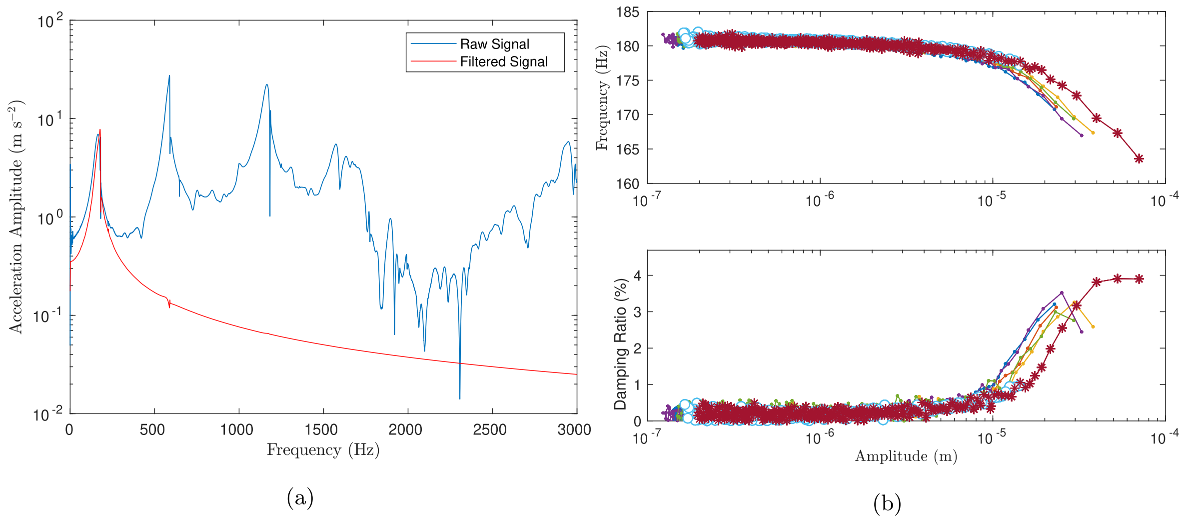

Fig. 16. Experimental results: (a) Frequency domain comparison for the bandpass filtering step; and (b) Identified modal characteristics; lines with asterices (∗) corresponds to high amplitude hit (others are medium level repeats).

Fig. 16a depicts a sample of the frequency content of the signal before and after the initial bandpass filtering step. Only the accelerometer data from the sensor in the side of the hammer is used for the current study.

Fig. 16b depicts the final modal characteristics after these are processed using the PFF technique. It can be observed that the frequencies start off from around 180 Hz, where the damping is very low (approximately 0.1 %), and then proceed to decrease gradually, while the damping increases by many folds. The largest amplitude hit is depicted using red lines with asterices ($*$). The experimental data are averaged and smoothened (using a Savitzky-Golay filter) to get a single characteristic line for each of the quantities.

4.2. Numerical implementation

4.2.1. Static prestress analysis

The static prestress analysis is conducted using 25 quadrature points in each element. This number was chosen in spite of the fact that lesser numbers were observed to work well too, since a threshold was observed in some cases below which it was prohibitively difficult to get the nonlinear solver to converge. All of the plots in this section are generated using a uniform coefficient of friction $\mu = 0.6$ throughout the interface [1].

Fig. 17 plots the resulting traction field on the interface, with the traction evaluated directly at the element centroids shown in Fig. 17a. This can be used as an indication about whether or not the element is in contact: if there is a non-zero traction developed, then the element is in contact. Elements with zero traction are left uncolored (white in the figure). It can be observed here that there are two large regions near the ends that are out of contact during the static loading. This can directly be correlated to the large values of the gap function (plotted in Fig. 11a) in these regions.

Fig. 17b to 17d plot out the colour maps of the nodal traction values in each direction interpolated in a least-squares sense. It must be noted that even though the normal tractions at the quadrature locations are strictly positive (as are the nodal forces), the least-squares solution will require nodal traction values to be negative in some regions. This is non-physical and a relic of the fact that the pressure variation in the interface cannot be easily captured by the finite element shape functions natively [2]. However, since the model in itself requires only integrals of these quantities, the integrals can be carried out accurately without this least-squares fit for the simulations (they were conducted only for the depictions). The absolute values of the interpolated normal pressures are plotted in Fig. 17b so that the features may be compared with the centroidal values in Fig. 17a.

As expected, it can be observed that there is very little to no slippage that occurs in the tangential directions (hence nominally zero tangential tractions in Fig. 17c to d). However, it can be observed that there are locations where there are considerable tangential kinematics that must not be ignored.

In order to understand the influence of the gap function and the uniformity of parameters (of the contact models used), two further simulations are conducted: (a) the interfaces are perfectly flat in the meso-scale, but have a non-uniformly distributed surface roughness (as characterized); and (b) the interfaces are perfectly flat and the roughness is uniform across the interface. Fig. 18a to b present the results of the two cases in order.

The first major ramification of assuming flat interfaces is that the regions in and out of contact are dramatically changed. Both Fig. 18a and b look relatively similar in the elements that are in contact. The influence of making the contact model uniform is that the interfacial traction becomes more uniform through the interface as can be observed by comparing the two figures.

Due to the way the model of the assembly was created, it was noted previously that the resulting model is singular since it does not impose any constraint on the rigid body mode corresponding to the two half beams separating along the bolt axis direction. However, upon application of the prestress, the perturbation model about the prestressed state does not possess this zero energy mode. In fact, the linearized eigen-modes of this perturbation state correspond to low amplitude modes of the assembled system.

Table 1 tabulates the linearized mode frequencies for the first mode for each of the above cases along with the experimental measurement. It can be observed that the flat, non0uniform case underpredicts the frequency by more than 12 Hz while the other cases are slightly better. Note that the apparent similarity between the "Flat; Uniform" case and the actual interface is only by chance; the parameters used here were taken from an element chosen in random and thus cannot be used to make further inferences. The relative closeness of all three modeling approaches gives confidence that this approach can be used for blind predictions on a structure that has not yet been fabricated.

4.2.2. Nonlinear dynamic analysis through CQSMA

As noted previously, the coefficient of friction is a persisting unknown in the formulation. For convenience, it is assumed to be uniform across the interface. Fig. 19 depicts the amplitude characteristics for different μ values. The abscissas of the plots are the amplitudes at the response locations (see Section 3.4).

A few observations can be made upon first glance:

- There is an offset of about 8 Hz in all the models for the low amplitude (nominally stuck case) in the frequency characteristics (see Fig. 19a).
- The coefficient of friction seems to determine the amplitude level characterizing the onset of slip-like behavior in the interface: for smaller values of μ, the onset of slip occurs at lower amplitudes (see Fig. 19b). Thus, for a given amplitude level, a smaller value of μ implies increased dissipation.

[1] Little to no appreciable change was observed for different values of μ for the prestress analysis

[2] This is the same reason that traction values evaluated at element centroids are better indicators of the contact state than the nodal quantities.

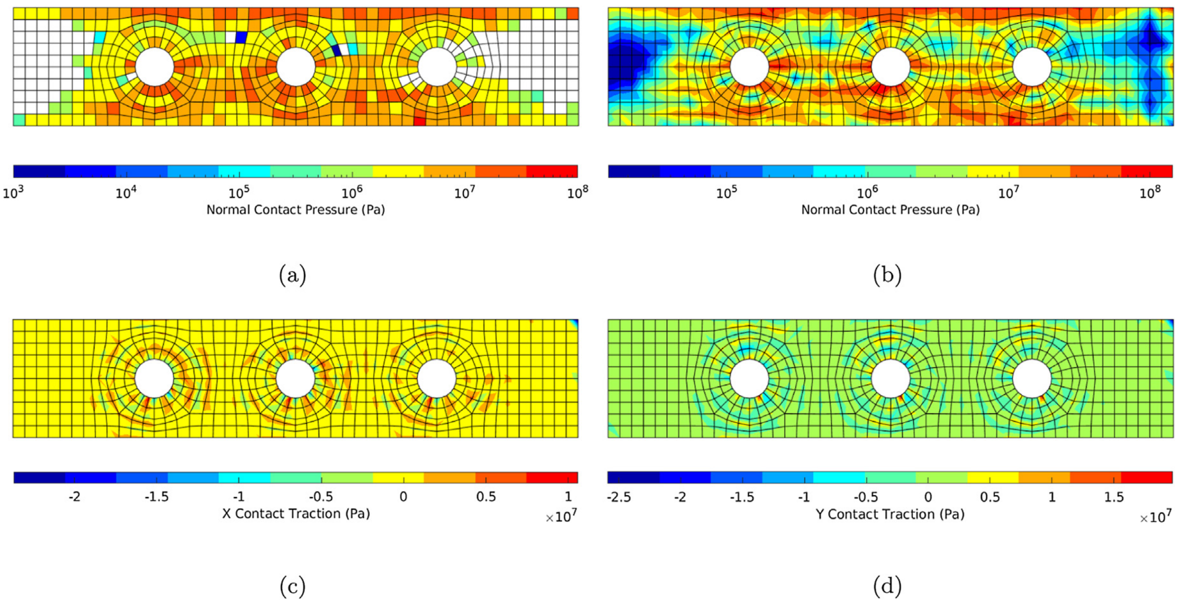

Fig. 17. Results of static prestress analysis: (a) Contact pressures at element centroids (empty elements indicate separation); (b) Interpolated normal contact pressure; (c) X-tangential contact pressure; and (d) Y-tangential contact pressure.

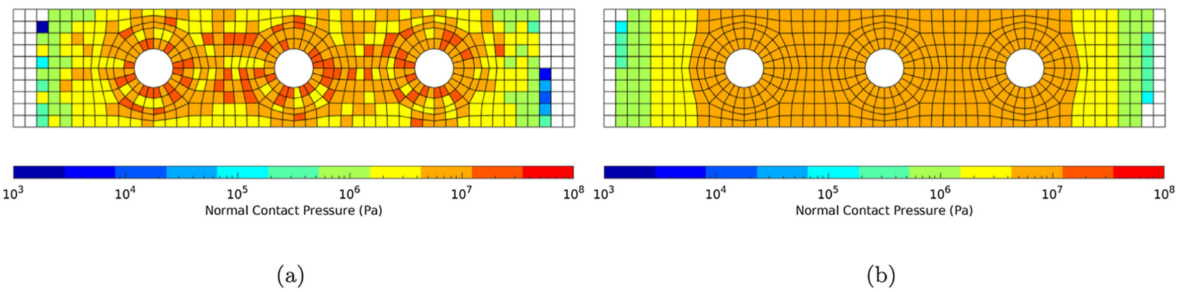

Fig. 18. Influence of flatness and non uniformity (empty elements indicate separation): (a) Flat interface with non uniform roughness; and (b) Flat interface with uniform roughness.

Table 1
Comparison of linearized mode-frequencies for the three different configurations studied here with the experimental prediction. The "Non-flat; Non-Uniform" case corresponds to the characterized interface.

Configuration	Mode Frequency (Hz)
Non-Flat, Non-uniform	174.21
Flat; Non-Uniform	168.91
Flat; Uniform	172.76
Experimental	**180.92**

- There seem to be two markedly different dissipative behaviors in the amplitude regime of interest: for $\mu < 0.20$, the dissipation characteristic seems to have a concave region in the region of interest and for $\mu \geqslant 0.20$, the characteristic seems to be more convex. This may be attributed to the "region" in the stick–slip transition the regime of interest lies in.
- Close to $\mu = 1.0$, the dissipation characteristics seem to converge to a particular curve (as seen by the 0.75 and 0.99 curves in Fig. 19b).
- The power-law slopes in the dissipation plot Fig. 19c do not seem to vary much over the different μ values. The implication even a small variation has on the response is however exemplified by the amount of variations the other two subplots seem to exhibit.

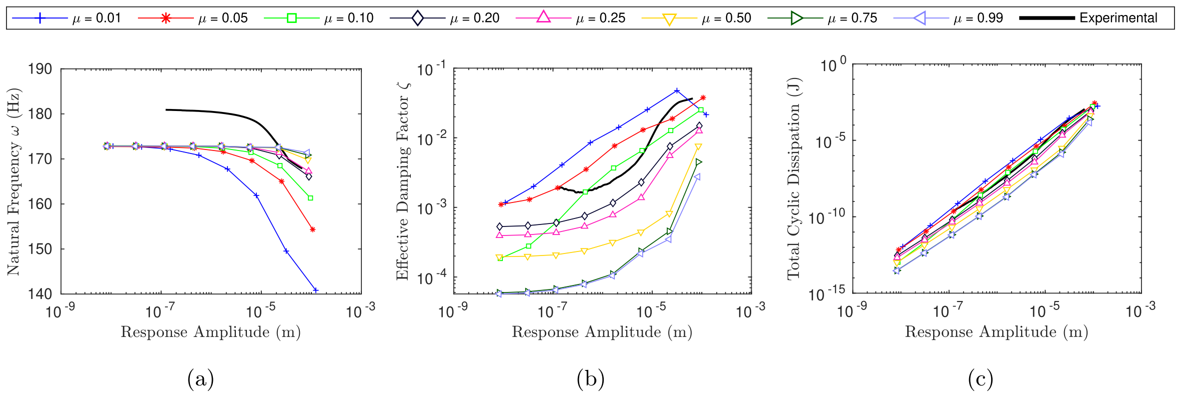

Fig. 19. Amplitude-Modal Characteristics for the first mode for different μ values: (a) Variation in natural frequency; (b) Variation in effective damping factor; and (d) Variation in cyclic dissipation.

The low amplitude offset may be attributed to several factors including persisting uncertainties in the bolt prestress, errors in the interfacial characterization, epistemic uncertainties in the contact models employed, etc (see Appendix A for some discussions). Coming to the contact model, it must be noted that the Hertzian solution presents an over-prediction of the normal traction (and hence the stiffness). Thus it is not realistic to expect a larger "true" stiffness here [3]. For the tangential contact model on the other hand, a standard form has been assumed for simplicity. Using more involved models (such as those in [25]) could offer possible improvements.

The observations on the influence of the coefficient of friction may be understood by visualizing the hysteretic behavior of the tangential oscillations. Consider a constant slip force-constant stiffness case as shown in Fig. 20. For a low coefficient of friction (red), the element starts dissipating at a much lower displacement amplitude as compared to an element with a higher friction coefficient (blue). By comparing different displacement amplitudes and where they lie with respect to the thresholds for each element, one it is obvious that even beyond the point where the second element starts slipping, there will be a certain threshold until which the first element will dissipate more. Since the interface consists of many such elements, the above observations may be corroborated with what would be expected from such a trend.

In order to understand the significance of the modal characteristics in Fig. 19, it is important to develop some insight into the hysteretic phenomena in the interface. This is done here by visualizing the dissipation fluxes through the interface. Fig. 21 plots the dissipation flux distribution over the interface for four different response (or forcing) levels along the modal backbone, signifying a nominally stuck level, a stick–slip-transition level, a nominally slipping level, and an unrealistically high level. Fig. 21a to c depict the numerical and experimental backbones in terms of the natural frequency, effective damping factor, and total dissipation (respectively) for $\mu = 0.2$ over a larger response amplitude level than in the previous figure.

The first feature that is readily apparent from the extended backbones (Fig. 21a to c) is that the behavior of the system post nominal slippage looks to be slightly more involved than that observed for Single Degree-Of-Freedom (SDOF) models with elastic friction. In SDOF models there exist distinct stuck and slipped frequencies with the transition between them being characterized as the nonlinear phenomenon. It has also previously been shown, since the slipped frequency is smaller than the stuck frequency, that the resulting damping factor will show a downward trend from the slipping point, which is also accompanied by a change in the power-law slope of the dissipation curve [78,79,49]. In the current application, although the dissipation and damping factor behaviors seem to be consistently reminiscent of the SDOF systems (Fig. 21b to c), the frequency shifts are not. The frequency seems to progressively decrease with the forcing level. It must however be noted that the amplitude levels in the right-most end of these plots are in the order of 1 m, which is an unrealistic scenario for the current application since it will result in the system incurring significant plastic deformation, but the results may be helpful for developing intuition about the underlying frictional phenomena.

Looking at the dissipation fluxes Fig. 21d to g, the first observation is that the magnitudes in the normal directions are several orders of magnitude lesser than that in the tangential directions. This is consistent with the fact that the normal contact model is perfectly elastic and no dissipation is expected to happen here. Due to the nature of the mode shape (see Section 3.4), relative translation on the interface is expected in the X direction only, and all Y directional effects will be due to Poisson effects alone, since the model is perfectly symmetric about the vertical plane (XZ plane). The influence of the Y dissipation, although much smaller than that of the X dissipation, are nonetheless considerable, as may be seen from the figures in all cases.

For Point 1 (Fig. 21d), the system is expected to be nearly linear since the amplitude level is extremely small. The interface however does dissipate, and this may be observed from the figure too. Most of this comes from slippage near the ends of the interface where the contact pressure is expected to be lesser since they are not directly under the bolts. Considering the pre-

[3] For non–Hertzian contact such as pin-in-hole or conformal contact, the elastic stiffness could be up to 25% higher than for the Hertzian case [16]

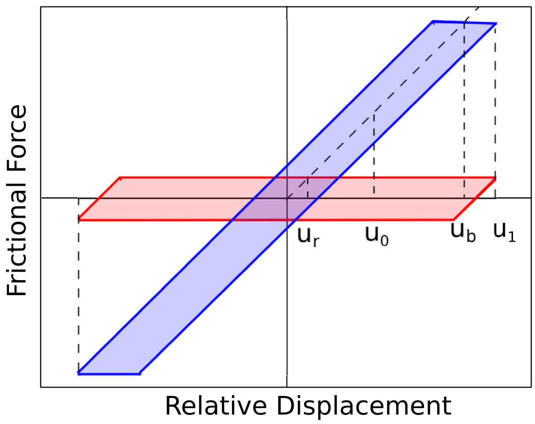

Fig. 20. Idealized hysteresis loops for a low μ (red) and a high μ (blue) element.

stress results (Fig 17), where it was remarked that a considerable region towards the ends is found to be out of contact as per the meso-interface gap function, the distribution of the *X* dissipation here appears similar (there is a low dissipation region near the ends).

Point 2 (Fig. 21e) corresponds to a response level just before the frequency makes a considerable "down-ward turn". It can be seen that the dissipation fluxes are now larger in magnitude and also that more regions are participating in the frictional interactions. This can be corroborated with the fact that the damping factor is steadily increasing around this level. An additional observation that can be made here pertains to the detection of nonlinearity. Looking at the frequency response alone, the system appears to still be in the near-linear regime, but the damping factor plot shows that the frictional nonlinearities are very much active at this point. From an identification perspective, this implies that the detection of dissipation nonlinearities will be a much more reliable way of characterizing bolted joints than frequency-shift nonlinearities.

At point 3 (Fig. 21f), the system may be said to be in a fully slipped condition, had this been an SDOF frictional element, since it is chosen at the peak of the damping factor curve and the point of slope-change in the power-law amplitude-dissipation slope. The flux distributions indicate that at this level, almost the complete interface is participating near-equally in the energy dissipation. This is characteristic of a nominally slipped state. The exact nature of the deflection is however not akin to macro-slip, but an expansion of the whole interface (left segment expands left-ward; right, right-ward; and center stays without expansion). There have been some recent studies that indicate that such behaviors can indeed be observed experimentally [8,9].

At point 4 (Fig. 21d), with an extremely high level of excitation (albeit non-physical for the current system), the dissipation flux distribution reveals that the interface is no longer being "utilized" in an equal fashion. Although there is dissipation throughout the interface, the amount of energy lost near the ends is much greater than that lost in the inner regions of the interface. This "loss of optimality" in the participation of different portions of the interface seems to be playing an important role in the shift of the dissipation power law slope which also characterizes nominal slippage. Further, since the interfacial separation is expected to occur in a much more drastic fashion, the simulation detects a significant amount of dissipation in the normal direction too. One must, however, not interpret this as something necessarily physical since one of the basic assumptions in the CQSMA procedure, i.e., that the mode shape may be assumed to remain constant over the operational regime, is clearly violated for these high amplitude levels. Further investigation is necessary to understand if these are merely numerical artifacts or if there is some underlying physics. Another aspect that must be taken into consideration at these large levels is bolt-pinning. Since no contact model is employed to capture the interaction of the hole and the bolt, the added stiffness due to the pinning of the bolt is not accounted for in the current model.

Since the Meso-scale topology characterization is prone to experimental error in the current setup, simulations are also conducted for the fully flat case, where the gap function is taken to be uniformly zero everywhere. The main purpose of this is to develop insights into the contribution of the gap function to the accuracy of the system level solution. An initial observation was made from the linearized frequency values in Section 4.2.1, where the "flattened" system seemed to show a reduced stiffness. Fig. 22 plots the results of this set of simulations in a format similar to the previous one. The differences are not appreciable for the modal characteristics plots due to the qualitative similarity of Figs. 22a to 22c their counterparts in Fig. 21a to c apart from the initial offset in the stuck frequency and some differences in the transition to slip region. However, the dissipation fluxes show a much more pronounced influence. This seems to suggest that the prediction of stiffness nonlinearities is a much easier problem than the prediction of dissipative nonlinearities for bolted joint applications, consistent with previous observations [1]. Although internal resonances are primarily driven by frequency shifts, it is the opinion of the current authors that accurate modeling of the non-dissipative components involved will be a much easier task than the modeling of dissipative components.

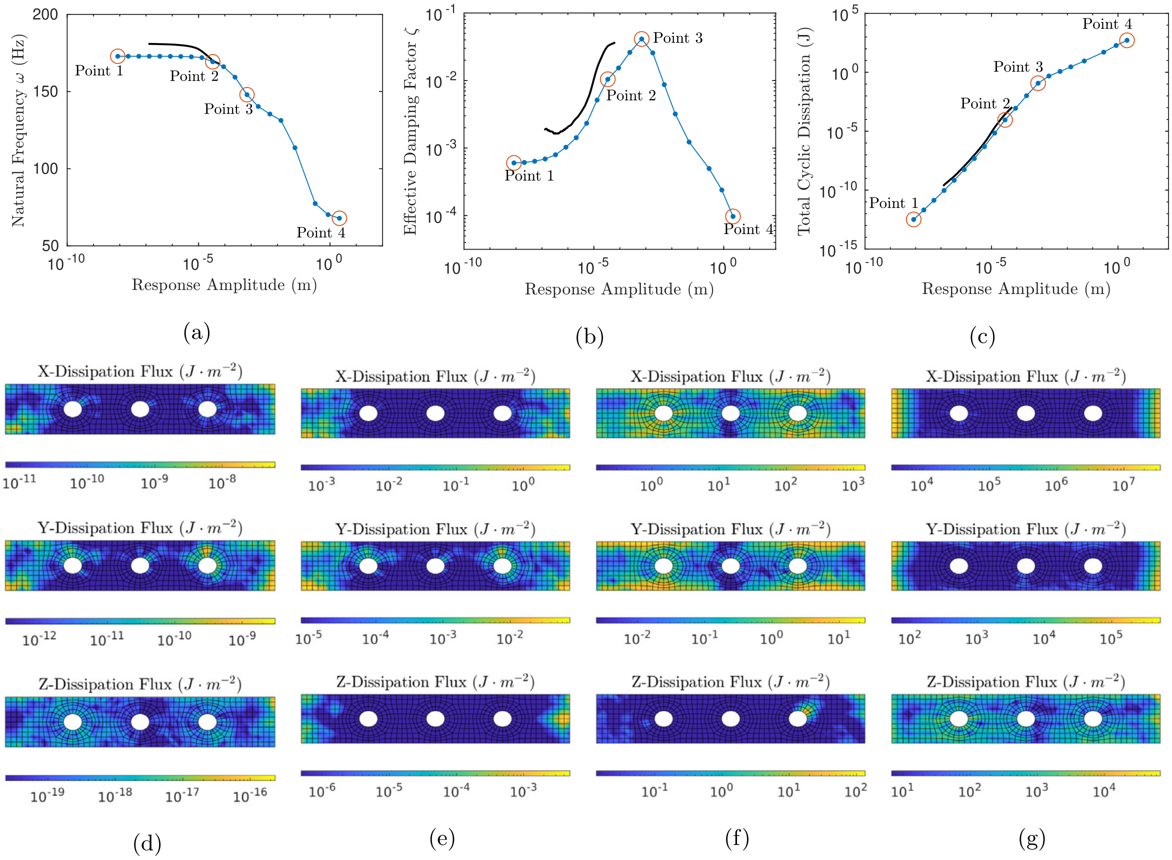

Fig. 21. Interfacial dissipation fluxes for different loading conditions for $\mu = 0.2$. (a)-(c) are the modal response characteristics (as in Fig. 19) over a broader response level range (dark continuous lines are experimental and the dotted blue ones are simulated curves); (d), (e), (f), and (g) are the dissipation fluxes plotted over the interface in the tangential (x and y) and normal (z) directions for forcing amplitudes corresponding to point 1, 2, 3, and 4 on (a)-(c) respectively.

Once again, four points are identified so that the results may be compared with the previous case. It can be seen that the qualitative understanding that maximal dissipation occurs when the entire interface participates near-equally in energy dissipation still seems to hold in this case. The exact regions of dissipation are, however, slightly different from the previous case, such as the absence of "gaps" near the ends of the structure, etc. These are mostly expected since the meso-scale irregularities seem to be the primary cause of these details.

4.3. Micro-scale trends

Irreversible changes in the tribological and topological properties of the interface may be interpreted as wear. In the current context, since the contact laws are all generated from the roughness parameters, it is now possible to isolate only the employed roughness parameters as the most relevant for modifying the response of the system. Further, since interfacial traction and dissipation fluxes can be thought of as the prime "drivers" of wear in the interface, the current section attempts to understand if it is possible to establish statistical correlations between these parameters and the interfacial parameters.

For this study, the experimental test procedure followed is,

1. Interfacial scan 1;
2. Assembly;
3. Bolt prestress;
4. 7 Hammer impact tests;
5. Disassembly;
6. Interfacial scan 2.

The whole procedure is completed in a single day within a span of about 5 h and thus it is very meaningful to look for possible correlations in the way interfacial parameters change between steps 1 and 6. The change in roughness ΔR_t, x- and y-radii β_X, β_Y, and the change in the estimated number of asperities per element are taken as the most critical "responses".

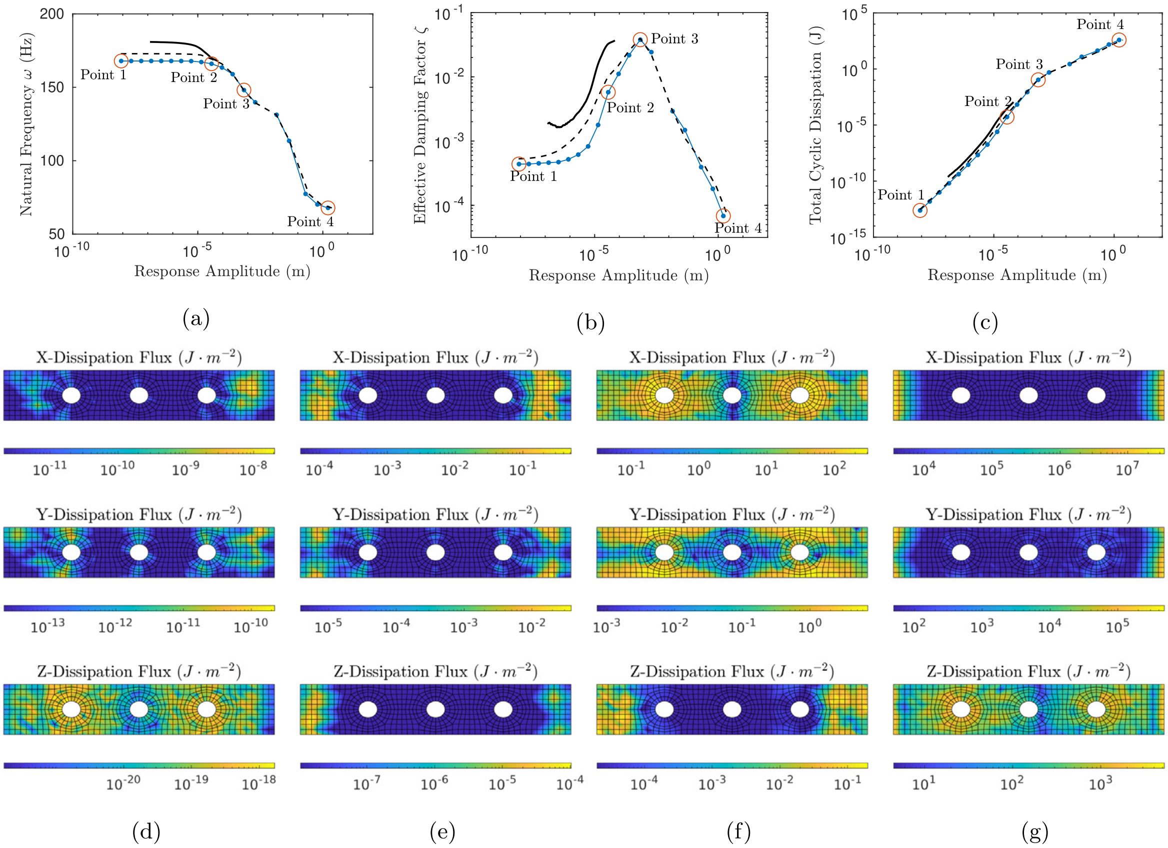

Fig. 22. Interfacial dissipation fluxes for different loading conditions for $\mu = 0.2$ for the fully flat interface. (a)-(c) are the modal response characteristics (as in Fig. 19) over a broader response level range (dark continuous lines are experimental and the dotted blue ones are simulated curves); Additionally the dark dashed lines represent the simulated responses for the non-flat interface case. (d), (e), (f), and (g) are the dissipation fluxes plotted over the interface in the tangential (x and y) and normal (z) directions for forcing amplitudes corresponding to point 1, 2, 3, and 4 on (a)-(c) respectively.

Since a considerable amount of experimental variability was observed for the gap function, this is omitted for the current study. The traction in the interface at the end of the prestress analysis T_n, and the total dissipation flux $D_x + D_y + D_z$ (see discussions in Section 4.2.2) at Points 1 and 2 in the response backbone (labeled as D_1 and D_2 respectively) are treated as the possible factors for the current study. Since an exhaustive treatment of correlation is not the purpose of the current work, a simplified approach is followed in order to gain insights for future work. A single value is calculated for each element in the interfacial mesh for the factors and parameters, and Spearman's correlation coefficient [80] is used to test for monotonic relationships between the factors and the responses. The null hypothesis for the test may be stated as,

$$H_0 : \text{There is no [monotonic]relationship between the factors and the responses[in the population]}. \tag{47}$$

The correlation coefficient ρ may be calculated for each factor-response pair and a p value may be estimated from this for a significance interpretation. ρ, bounded between -1 and +1, denotes the amount of relationship, i.e., values close to ± 1 denote strong monotonic (increasing or decreasing) tendencies, while values closer to 0 indicate a smaller relationship. The results are interpreted with a significance level of 0.05, so that there is a confidence of 95% to reject the null hypothesis.

Tables 2a to 2b summarize the results of the analysis. As already mentioned, the current approach for characterizing the gap function is prone to errors and thus factors calculated from a fully flat (but non-uniform roughness) simulation are also studied for correlation, and are super-scripted with f. From the p values, it can be seen that the null hypothesis may not be rejected for most of the cases. This can imply either that the current set of factors are insufficient or that the data is not precise enough (as the resolution is only $30\,\mu\text{m} \times 50\,\mu\text{m} \times 0.5\mu\text{m}$ in the x, y, and z directions). However, for the changes in roughness, there seem to be significant confidences in rejecting the null hypothesis pertaining to the normal traction and dissipation flux. This trend is observed identically for the simulations with and without the gap function. Comparing the numbers in the two cases, it appears that there are slightly stronger correlations and higher confidences in the relationships for the latter case. Other than this, there are high confidence results for two other pairs, namely, $\left(T_n, \Delta\widehat{N}\right)$ and $\left(D_1^f, \Delta\beta_X\right)$.

From the above discussions and the actual values of ρ, the following comments may now be made about the statistically significant cases.

Table 2
Results of Spearman correlation tests: (a) Spearman ρ; and (b) the corresponding p values. Cases where the null hypothesis may be rejected with a confidence of more than 95% are highlighted with boxes. Superscripts f denote the flat interface factors.

	ΔR_t	$\Delta\beta_X$	$\Delta\beta_Y$	$\Delta\widehat{N}$
(a)				
T_n	$\boxed{0.0822}$	−0.0578	0.0393	$\boxed{-0.1534}$
D_1	−0.0670	0.0615	−0.0253	0.0533
D_2	$\boxed{-0.0829}$	0.0507	−0.0361	0.0322
T_n^f	$\boxed{0.1528}$	−0.0462	0.0345	−0.0408
D_1^f	−0.0365	$\boxed{-0.0810}$	−0.0411	0.0156
D_2^f	$\boxed{-0.0862}$	0.0036	−0.0261	0.0502
(b)				
T_n	$\boxed{0.0463}$	0.1616	0.3411	$\boxed{0.0002}$
D_1	0.1046	0.1364	0.5395	0.1969
D_2	$\boxed{0.0445}$	0.2197	0.3819	0.4350
T_n^f	$\boxed{0.0002}$	0.2632	0.4041	0.3236
D_1^f	0.3767	$\boxed{0.0497}$	0.3202	0.7051
D_2^f	$\boxed{0.0368}$	0.9315	0.5282	0.2244

- Since both $\rho(T_n, \Delta R_t)$ as well as $\rho\left(T_n^f, \Delta R_t\right)$ are greater than zero, this indicates that the interfacial roughness may have an increasing relationship with the traction experienced at the end of bolt tightening.
- Both $\rho(D_2, \Delta R_t)$ as well as $\rho\left(D_2^f, \Delta R_t\right)$ are less than zero, implying that greater operational dissipation through a region may be correlated with a decrease in the roughness there.

Similar interpretations also follow for $\rho\left(T_n, \Delta\widehat{N}\right)$ and $\rho(D_2, \Delta\beta_X)$, which have also turned out to be statistically significant relationships. All of the correlation coefficients are very small in magnitude, indicating that the onset of wear is typically very gradual for experiments similar to the current set.

5. Discussions and conclusions

The specific contributions of this work are,

- A multi-scale roughness-based compliant interface model has been formulated for interfaces in contact. Relationships are drawn from rough contact theory to establish the exact form of the model and it is implemented in a traction-consistent manner using interfacial zero-thickness elements (Section 2.1, 2.2).
- The approach is demonstrated to lend itself to applications involving minor deviations in the initial surface that can be expressed in the form of gap functions (Section 2).
- The hysteretic contact laws are implemented in an incremental quasi-static formulation that is derived as a representation of the rate-dependent form of the nonlinearities (Section 2.2.2). This makes the implementation convenient for modal quasi-static analysis approaches.
- The use of null-space reductions to remove the zero energy modes of bolted structures in the fully free configuration has been introduced rigorously, which will be helpful for conducting nonlinear analyses have been highlighted (Section 3.1.1).
- Coupled quasi-static modal analysis, an improved formulation of QSMA [15] has been formulated and successfully employed for the benchmark implementation (Section 3.1.2). The current improvement, referred to in the text as CQSMA has the following key differences from QSMA,
  - It makes the implementation of nonlinear interfacial laws mathematically consistent. QSMA solves for the linearized perturbations about the prestress solution, while CQSMA solves for the actual displacements.
  - It makes it possible to account for prestressing and dynamic loading in a coupled fashion. By formulation, QSMA had a fully decoupled static simulation step followed by the modal excitation step, while CQSMA conducts both simultaneously, in a way that is more consistent with reality.
- A repeatable procedure has been used for pre-stressing the bolts using strain gauges to monitor the axial extension of the bolts (Section 3.3).
- Different response regimes of a bolted joint structure are highlighted using a benchmark structure through modal characteristic plots and interfacial dissipation flux distribution maps (Section 4.2.2).
- It is demonstrated that micro-scale trends may be successfully studied through statistical means in order to characterize correlations between simulated factors and experimentally measured parameters (Section 4.3).

The main drawback in the current study comes from experimental limitations introduced by the laser profilometer set up. Since no mechanism has been used for ensuring perpendicularity of the scanning beam and the interfacial surface, the meso-scale topology (in the form of the gap-function) may be interpreted only as a shifted and/or rotated representation of its actual counterpart. Also, an increased resolution scanning apparatus such as a confocal microscope [81–83] would also greatly improve the confidences in the correlation analyses.

In the computational modeling side, the system must be investigated using transient and steady state harmonic methods in order to gain a deeper understanding of the "true" nonlinear dynamical behavior of the system in an actual application scenario. A more consistent rough contact formulation arising either out of a reduced non-parametric representation of the expectation statistics, or through controlled machining processes yielding more repeatable roughness distributions, could greatly improve the connect between model and reality. Further, in the asperity level, the employed constitutive model corresponds to a simple Hertzian contact case in the current work. More advanced models could be employed so as to capture the influence of adhesion (see Section 3.2.1), plasticity, fracture, etc., that could reduce epistemic uncertainties. Another key drawback in the current formulation is that no relationships have been employed for fixing the coefficient of friction μ. More physics-based methods of estimating this parameter will greatly reduce the epistemic uncertainties in the formulation, since its influence on the dissipation properties has been demonstrated to be extremely significant. Application of the friction modeling approach for large displacement contact problems has to be investigated in detail since the simplified ZTE formulation will no longer be valid for such cases and interpretations of the rough contact parameters will have to be revised.

Lastly, it must be noted that most experimental studies of jointed systems document significant variability in the observations [77] (seen to a limited extent in Section 4.1), often cited to be due to friction or variations in preload. There have been several stochastic modeling approaches applied to such systems with varying successes [84–86]. It would be relevant to construct stochastic rough contact models in order to account for such variability from the perspective of uncertainty quantification methods.

Going forward, generalizing the approach to minimize the use of exhaustive interfacial scans can expand the applicability to scenarios where such scans are practically impossible. A possible approach to this would be to establish a consistent way of working back the asperity distributions on a surface based on machining processes and documented surface finishes. Since most industrial components are machined to conform to standard specifications, conducting parametric studies on the relationship of these specifications to the rough contact parameters would add significant value to such studies.

Declaration of Competing Interest

The authors declare that they have no known competing financial interests or personal relationships that could have appeared to influence the work reported in this paper.

Acknowledgements

The authors thank Mianmian Ruan for helpful assistance for the bolt preparation; and Mengshi Jin for helpful discussions regarding the ringdown data processing.

Funding: The authors are thankful for the support of the National Science Foundation under Grant No. 1744327 and the China Scholarship Council (CSC).

Appendix A. Sources of Variability in the low-amplitude natural frequency

The current section seeks to provide an explanation about the offset in the natural frequency for low amplitudes where the benchmark system seems to behave linearly. In Section 4.2.2 (see Table 1 and Fig. 19), the predicted low amplitude frequency is 174.21 Hz while the experimental value is 180.92 Hz. Two sources of variability are investigated here: (a) additional stiffening provided by the bungee supports; and (b) variability in the bolt strains measured from the strain gauges.

For studying the amount of frequency offset introduced by the bungee cables, the appropriate regions of the assembly are first identified as surface sets on the finite element model (see Fig. 23) and then virtual nodes are used to represent these using distributing coupling elements. These virtual nodes are connected to the ground using linear stiffnesses estimated assuming that the bungee cords themselves may be approximated as rigid during operation. Since the total mass of the assembly is 3.68 kg and each bungee cord, suspended at about two feet length (0.6096 m), supports approximately half of the total weight, the (low-amplitude oscillatory) pendulum stiffness is

$$k_{pend} = \frac{m_a}{2}\frac{g}{l} \approx 30Nm^{-1}. \tag{48}$$

As the focus of this study is to determine the effect of the bungee cord stiffness on the natural frequencies of the flexible body modes, a simplified analysis is utilized in which the interface is modeled with hard contact and ideal Coulomb friction in ABAQUS. Table 3 shows the natural frequencies of the first 10 elastic modes of the system (mode 1 has been the focus of

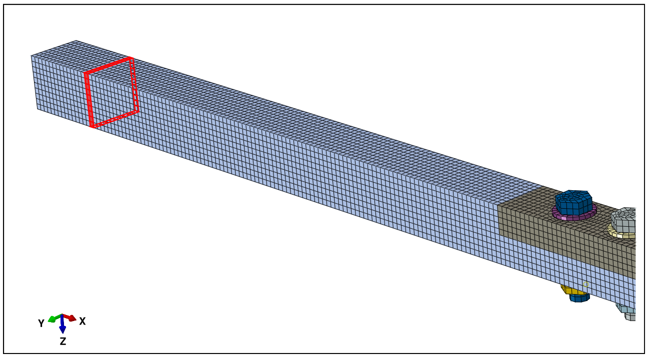

Fig. 23. Surface set used to enforce the bungee stiffness as boundary condition.

Table 3
Influence of boundary condition model on linearized natural frequencies.

Mode	Free-Free B.C. Natural freq (Hz)	Bungee cord B.C. Natural freq (Hz)
1	167.42	167.42
2	227.31	227.31
3	585.22	585.22
4	666.10	666.10
5	1194.7	1194.7
6	1272.5	1272.5
7	1608.0	1608.0
8	1685.1	1685.1
9	2030.8	2030.8
10	2862.6	2862.6

Table 4
Influence of bolt prestress on the linearized natural frequency and Percentage area in contact for the non-flat + measured roughness and the flat + measured roughness models. The case used for all the studies in the paper (corresponding to 2050 $\mu\epsilon$) is boxed in black.

Bolt strain	Bolt Load	Non-flat + measured rough surface		Flat + measured rough surface	
($\mu\epsilon$)	(kN)	Nat. Freq. (Hz)	Contact area (%)	Nat. Freq. (Hz)	Contact area (%)
1050		172.62	62.16	165.34	86.7904
1250		170.13	67.41	167.17	86.7904
1550		173.39	72.27	166.46	87.8913
1750		174.36	74.35	167.72	88.5517
$\boxed{2050}$		174.21	77.59	168.98	89.8727
2250		174.07	79.45	168.57	90.3130
2500		173.33	81.05	168.77	91.1936
2750		173.44	81.72	169.10	91.1936
3000		172.54	82.47	170.12	91.1936

all the studies in this paper). It can be observed that there is no appreciable change to the first two decimal places, showing that it is not possible to obtain a 6 Hz shift due to the bungees alone.

The second consideration, involving possible errors in the strain measurements, is investigated by conducting the linearization about the prestress state of various bolt strain levels. Table 4 tabulates the mode 1 natural frequencies and percentage contact area for different bolt strain levels (in an approximately $\pm 50\%$ band). Two cases of contact models developed from the surface measurements, one with the non-flat surface with measured roughness, and the other with the assumption that the nominal surface is perfectly flat. It can be seen that the variation in natural frequency with the prestress level in the first case does not seem to be gradual or monotonic. For the second case however, the natural frequency is observed to be monotonically increasing with the bolt prestress level until the frequency saturates at 25 kN. These observations may be corroborated with the trends in the area in contact.

Fig. 24 depicts these trends graphically, wherein it may be observed that the non-flat interface nominally has much smaller area in contact for any given prestress level. This shows that the exact topology of the interface has a highly non-trivial and significant impact on the area in contact, which is extremely important to the response of the system. Erroneous meso-surface identification is thus a factor that may not be ruled out as a possible cause for the offset seen.

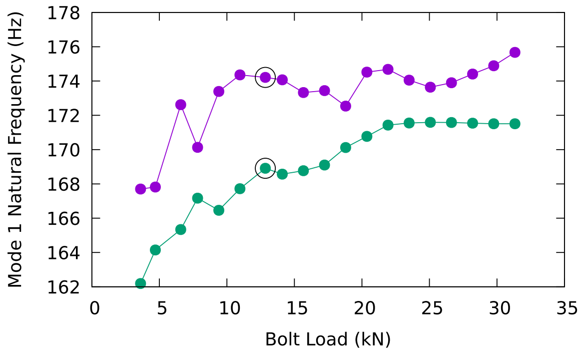

(a)

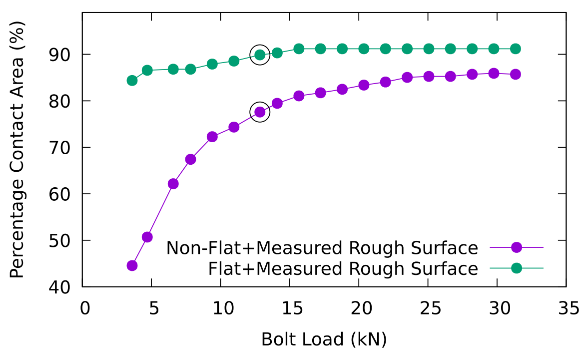

(b)

Fig. 24. Influence of Bolt load (per bolt) on (a) linearized natural frequency; and (b) percentage area of contact. The case used for all the studies in the paper (corresponding to 2050 $\mu\epsilon$) is encircled in black.

References

[1] D.J. Segalman, D.L. Gregory, M.J. Starr, B.R. Resor, M.D. Jew, J.P. Lauffer, and N.M. Ames. Handbook on Dynamics of Jointed Structures. Technical Report SAND2009-4164. Sandia National Laboratories, Albuquerque, NM, 2009..

[2] S.A. Nassar, A. Abboud, An improved stiffness model for bolted joints, J. Mech. Des. 131 (12) (2009) 121001, https://doi.org/10.1115/1.4000212, ISSN 1050-0472.

[3] S.A. Nassar, S. Ganeshmurthy, R.M. Ranganathan, G.C. Barber, Effect of tightening speed on the torque-tension and wear pattern in bolted connections, J. Pressure Vessel Technol. 129 (3) (2006) 426–440, https://doi.org/10.1115/1.274929, ISSN 0094-9930.

[4] S.A. Nassar, P.H. Matin, G.C. Barber, Thread friction torque in bolted joints, J. Pressure Vessel Technol. 127 (4) (2005) 387–393, https://doi.org/10.1115/1.2042474, ISSN 0094-9930.

[5] M. Ruan. The variability of strains in bolts and the effect on preload in jointed structures. Master's thesis, Department of Mechanical Engineering, Rice University, Houston, TX, May 2019..

[6] A. Pazouki, M. Kwarta, K. Williams, W. Likos, R. Serban, P. Jayakumar, D. Negrut, Compliant contact versus rigid contact: a comparison in the context of granular dynamics, Phys. Rev. E 96 (4) (2017), https://doi.org/10.1103/PhysRevE.96.042905, ISSN 2470-0045, 2470-0053.

[7] B. Seeger, P. Butaud, F. Du, V. Baloglu, M.R.W. Brake, C.W. Schwingshackl. In situ measurements of interfacial contact pressure during impact hammer tests, in: 36th International Modal Analysis Conference (IMAC XXXVI), Orlando, FL, February 2018..

[8] Wei Chen, Mengshi Jin, Iyabo Lawal, Matthew R.W. Brake, Hanwen Song, Measurement of slip and separation in jointed structures with non-flat interfaces, Mech. Syst. Signal Process. 134 (2019) 106325.

[9] S.W.B Klaassen, M. Brøns, G. Chauda, T.A. Kasper, C.W. Schwingshackl, M.R.W. Brake. Optical full field monitoring of bolted lap-joint behaviour under vibration, in: 37th International Modal Analysis Conference (IMAC XXXVII), Orlando, FL, January 2019..

[10] L. Bureau, T. Baumberger, C. Caroli, Contact mechanics for randomly rough surfaces, Eur. Phys. J. E 19 (2) (2006) 163–169, https://doi.org/10.1140/epje/e2006-00019-2, ISSN 1292-8941, 1292–895X. http://arxiv.org/abs/cond-mat/0510232. arXiv: cond-mat/0510232.

[11] H. Ghaednia, X. Wang, S. Saha, Y. Xu, A. Sharma, R.L. Jackson, A review of elastic-plastic contact mechanics, Appl. Mech. Rev. 69 (6) (2017), https://doi.org/10.1115/1.4038187, 060804–060804-30, ISSN 0003–6900.

[12] X. Lei, How do asperities fracture? An experimental study of unbroken asperities, Earth Planet. Sci. Lett. 213 (3) (2003) 347–359, https://doi.org/10.1016/S0012-821X(03)00328-5, ISSN 0012-821X.

[13] A. Fantetti, L.R. Tamatam, M. Volvert, I. Lawal, L. Liu, L. Salles, M.R.W. Brake, C.W. Schwingshackl, D. Nowell, The impact of fretting wear on structural dynamics: experiment and simulation, Tribol. Int. 138 (2019) 111–124.

[14] M. Krack, L. Salles, F. Thouverez, Vibration prediction of bladed disks coupled by friction joints, Arch. Comput. Methods Eng. 24 (3) (2017) 589–636, https://doi.org/10.1007/s11831-016-9183-2, ISSN 1134-3060, 1886–1784.

[15] R.M. Lacayo, M.S. Allen, Updating structural models containing nonlinear Iwan joints using quasi-static modal analysis, Mech. Syst. Signal Process. 118 (2019) 133–157, https://doi.org/10.1016/j.ymssp.2018.08.034, ISSN 08883270.

[16] K.L. Johnson, Contact Mechanics, Cambridge University Press, Cambridge, 1985.

[17] M.R.W. Brake, An analytical elastic plastic contact model with strain hardening and frictional effects for normal and oblique impacts, Int. J. Solids Struct. 62 (2015) 104–123.

[18] A. Signorini, Questioni di elasticit non linearizzata e semilinearizzata (Topics in non linear and semi linear elasticity), Rendiconti di Matematica e delle sue Applicazioni 5 (18) (1959) 95–139.

[19] G. Fichera, Boundary Value Problems of Elasticity with Unilateral Constraints, in: C. Truesdell (Ed.), Linear Theories of Elasticity and Thermoelasticity, Springer, Berlin Heidelberg, Berlin, Heidelberg, 1973, pp. 391–424, https://doi.org/10.1007/978-3-662-39776-3_4, ISBN 978-3-662-38853-2 978-3-662-39776-3.

[20] R.L. Jackson, I. Green, On the modeling of elastic contact between rough surfaces, Tribol. Trans. 54 (2011) 300–314.

[21] J.A. Greenwood, J.B.P. Williamson, Contact of nominally flat surfaces, Proc. R. Soc. London, Series A 295 (1966) 300–319.

[22] S. Medina, D. Nowell, D. Dini, Analytical and numerical models for tangential stiffness of rough elastic contacts, Tribol. Lett. 49 (1) (2013) 103–115, https://doi.org/10.1007/s11249-012-0049-y, ISSN 1023-8883, 1573–2711.

[23] C. Campana, B.N.J. Persson, M.H. Müser, Transverse and normal interfacial stiffness of solids with randomly rough surfaces, J. Phys.: Condensed Matter 23 (2011) 085001.

[24] M. Eriten, A.A. Polycarpou, L.A. Bergman, Physics-based modeling for fretting behavior of nominally flat rough surfaces, Int. J. Solids Struct. 48 (2011) 1436–1450.

[25] M. Eriten, A.A. Polycarpou, L.A. Bergman, Physics-based modeling for partial slip behavior of spherical contacts, Int. J. Solids Struct. 47 (18) (2010) 2554–2567, https://doi.org/10.1016/j.ijsolstr.2010.05.017, ISSN 0020-7683. DOI: http://www.sciencedirect.com/science/article/pii/S0020768310001952.

[26] E. Popova, V.L. Popov, The research works of Coulomb and Amontons and generalized laws of friction, Friction 3 (2) (2015) 183–190, https://doi.org/10.1007/s40544-015-0074-6, ISSN 2223-7690, 2223–7704.

[27] A. Visintin. The Science of Hysteresis Volume 1, chapter Mathematical Models of Hysteresis, pages 1–123. Elsevier Inc., 2005..

[28] M.A. Janaideh, R. Naldi, L. Marconi, P. Krejci, A hybrid model for the play hysteresis operator, Phys. B (2013).
[29] G.M. Jenkins, Analysis of the stress-strain relationships in reactor grade graphite, Br. J. Appl. Phys. 13 (1962) 30–32.
[30] S. Zucca, C.M. Firrone, M.M. Gola, Modeling underplatform dampers for turbine blades: a refined approach in the frequency domain, J. Vib. Control 19 (2013) 1087–1102.
[31] A.T. Mathis, N.N. Balaji, R.J. Kuether, A.R. Brink, M.R.W. Brake, and D.D. Quinn. A review of damping models for structures with mechanical joints. Applied Mechanics Reviews, Under review..
[32] M.L. Raffa, F. Lebon, G. Vairo, Normal and tangential stiffnesses of rough surfaces in contact via an imperfect interface model, Int. J. Solids Struct. 87 (2016) 245–253, https://doi.org/10.1016/j.ijsolstr.2016.01.025, ISSN 00207683.
[33] C. Putignano, L. Afferrante, G. Carbone, G. Demelio, A new efficient numerical method for contact mechanics of rough surfaces, Int. J. Solids Struct. 49 (2012) 338–343.
[34] S. Akarapu, T. Sharp, M.O. Robbins, Stiffness of contacts between rough surfaces, Phys. Rev. Lett. 106 (2011) 204301.
[35] W.R. Chang, I. Etsion, D.B. Bogy, An elastic-plastic model for the contact of rough surfaces, ASME J. Tribol. 109 (1987) 257–263.
[36] W.D. Iwan, On a class of models for the yielding behavior of continuous and composite systems, ASME J. Appl. Mech. 34 (1967) 612–617.
[37] D.J. Segalman, A four-parameter Iwan model for lap-type joints, J. Appl. Mech. 72 (5) (2005) 752–760.
[38] R.E. Goodman, R.L. Taylor, T.L. Brekke, A model for the mechanics of jointed rock, J. Soil Mech. Found. Division 94 (3) (1968) 637–660.
[39] H. Festjens, G. Chevallier, J.-L. Dion, A numerical tool for the design of assembled structures under dynamic loads, Int. J. Mech. Sci. 75 (2013) 170–177.
[40] N.N. Balaji, M.R.W. Brake, Systems and Signal Processing 126 (2019) 42–64, https://doi.org/10.1016/j.ymssp.2019.02.013, ISSN 0888-3270.
[41] M. Jin, M.R.W. Brake. Nonlinear system identification methods for jointed structures, in: 37th International Modal Analysis Conference (IMAC XXXVII), Orlando, FL, January 2019..
[42] M. Jin, M.R.W. Brake, H. Song. Comparison of nonlinear system identification methods for free decay measurements with application to jointed structures. J. Sound Vib., In press..
[43] M. Mayer, L. Gaul, Modeling of contact interfaces using segment-to-segment-elements for FE vibration analysis, in: 23rd International Modal Analysis Conference (IMAC XXIII), Bethel, CT, 2005.
[44] R.D. Mindlin, Compliance of elastic bodies in contact, ASME J. Appl. Mech. 16 (1949) 259–268.
[45] R.D. Mindlin, H. Deresiewicz, Elastic spheres in contact under varying oblique forces, ASME J. Appl. Mech. 20 (1953) 327–344.
[46] C. Cattaneo. Sul contatto di due corpi elastici: Distribuzione locale degli sforzi. Rendiconti dell'Accademia Nazionale dei Lincei, 27: 342–348, 434–436, 474–478, 1938..
[47] M. Afzal, I. Lopez Arteaga, L. Kari, An analytical calculation of the Jacobian matrix for 3d friction contact model applied to turbine blade shroud contact, Comput. Struct. 177 (2016) 204–217, https://doi.org/10.1016/j.compstruc.2016.08.014, ISSN 00457949.
[48] K.D. Hjelmstad, Fundamentals of structural mechanics, Springer Science & Business Media, 2007.
[49] M.R.W. Brake (Ed.), The Mechanics of Jointed Structures, Springer, 2017.
[50] B. Yang, T.A. Laursen, X. Meng, Two dimensional mortar contact methods for large deformation frictional sliding, Int. J. Numer. Meth. Eng. 62 (9) (2005) 1183–1225, https://doi.org/10.1002/nme.1222, ISSN 0029-5981, 1097–0207.
[51] L. Pesaresi, J. Armand, C.W. Schwingshackl, L. Salles, W. Wong, An advanced underplatform damper modelling approach based on a microslip contact model, Journal of Sound and Vibration (2018), https://doi.org/10.1016/j.jsv.2018.08.014, ISSN 0022-460X.
[52] K.G. Sharma, C.S. Desai, Analysis and implementation of thin-layer element for interfaces and joints, J. Eng. Mech. 118 (12) (1992) 2442–2462, https://doi.org/10.1061/(ASCE)0733-9399(1992)118:12(2442), ISSN 0733-9399, 1943–7889.
[53] X. Wang, L.B. Wang, Continuous interface elements subject to large shear deformations, Int. J. Geomech. 6 (2) (2006) 97–107, https://doi.org/10.1061/(ASCE)1532-3641(2006)6:2(97), ISSN 1532-3641, 1943–5622.
[54] P. Wriggers, J. Schröder, A. Schwarz, A finite element method for contact using a third medium, Comput. Mech. 52 (4) (2013) 837–847, https://doi.org/10.1007/s00466-013-0848-5, ISSN 0178-7675, 1432–0924.
[55] G. Beer, An isoparametric joint/interface element for finite element analysis, Int. J. Numer. Meth. Eng. 21 (4) (1985) 585–600, https://doi.org/10.1002/nme.1620210402, ISSN 0029-5981, 1097–0207.
[56] D.A.H. Hanaor, Y. Gan, I. Einav, Contact mechanics of fractal surfaces by spline assisted discretisation, Int. J. Solids Struct. 59 (2015) 121–131, https://doi.org/10.1016/j.ijsolstr.2015.01.021, ISSN 00207683.
[57] R. Buczkowski, M. Kleiber, Elasto-plastic interface model for 3d-frictional orthotropic contact problems, Int. J. Numer. Meth. Eng. 40 (4) (1997) 599–619, https://doi.org/10.1002/(SICI)1097-0207(19970228)40:4<599::AID-NME81>3.0.CO;2-H, ISSN 1097-0207.
[58] R. Jedynak, Exact and approximate solutions of the infinite integrals of the asperity height distribution for the Greenwood-Williamson and the Greenwood-Tripp asperity contact models, Tribol. Int. 130 (2019) 206–215, https://doi.org/10.1016/j.triboint.2018.09.009, ISSN 0301679X.
[59] M. Eriten, D.T. Petlicki, A.A. Polycarpou, L.A. Bergman, Influence of friction and adhesion on the onset of plasticity during normal loading of spherical contacts, Mech. Mater. 48 (2012) 26–42, https://doi.org/10.1016/j.mechmat.2012.01.003, ISSN 0167-6636.
[60] L. Gaul, M. Mayer. Efficient modelling of contact interfaces of joints in built-up structures, in: Computer Methods and Experimental Measurements for Surface Effects and Contact Mechanics VIII, volume I, pages 195–205, The New Forest, UK, May 2007. WIT Press. ISBN 978-1-84564-073-6. DOI: 10.2495/SECM070191. http://library.witpress.com/viewpaper.asp?pcode=SECM07-019-1..
[61] C. Siewert, L. Panning, J. Wallaschek, C Richter, Multiharmonic forced response analysis of a turbine blading coupled by nonlinear contact forces, J. Eng. Gas Turbines Power 132 (8) (2010) 082501, https://doi.org/10.1115/1.4000266, ISSN 07424795.
[62] J. Królikowski, J. Szczepek, Assessment of tangential and normal stiffness of contact between rough surfaces using ultrasonic method, Wear 160 (2) (1993) 253–258, https://doi.org/10.1016/0043-1648(93)90428-O, ISSN 00431648.
[63] N. Yoshioka, C.H. Scholz, Elastic properties of contacting surfaces under normal and shear loads: 1 Theory, J. Geophys. Res. 94 (B12) (1989) 17681, https://doi.org/10.1029/JB094iB12p17681, ISSN 0148-0227.
[64] N. Yoshioka, C.H. Scholz, Elastic properties of contacting surfaces under normal and shear loads: 2 Comparison of theory with experiment, J. Geophys. Res. 94 (B12) (1989) 17691, https://doi.org/10.1029/JB094iB12p17691, ISSN 0148-0227.
[65] H.A. Sherif, S.S. Kossa, Relationship between normal and tangential contact stiffness of nominally flat surfaces, Wear 151 (1) (1991) 49–62, https://doi.org/10.1016/0043-1648(91)90345-U, ISSN 0043-1648.
[66] M. Gonzalez-Valadez, A. Baltazar, R.S. Dwyer-Joyce, Study of interfacial stiffness ratio of a rough surface in contact using a spring model, Wear 268 (3) (2010) 373–379, https://doi.org/10.1016/j.wear.2009.08.022, ISSN 0043-1648.
[67] A. Poganik, M. Kalin, How to determine the number of asperity peaks their radii and their heights for engineering surfaces: A critical appraisal, Wear 300 (1–2) (2013) 143–154, https://doi.org/10.1016/j.wear.2013.01.105, ISSN 00431648.
[68] A. Horwitz. Ellipses Inscribed in Parallelograms. arXiv:0808.0297 [math], August 2008. http://arxiv.org/abs/0808.0297. arXiv: 0808.0297..
[69] A. Horwitz. Dynamics of ellipses inscribed in quadrilaterals. arXiv:1505.01048 [math], May 2015. http://arxiv.org/abs/1505.01048. arXiv: 1505.01048..
[70] B. Braden, The Surveyor's area formula, College Mathematics J. 17 (4) (1986) 326–337, https://doi.org/10.1080/07468342.1986.11972974, ISSN 0746-8342.
[71] O.C. Zienkiewicz, R.L. Taylor, The Finite Element Method for Solid and Structural Mechanics, The Finite Element Method, Elsevier Science, 2013, ISBN 9780080951362.
[72] L. Kogut, I. Etsion, Adhesion in elastic-plastic spherical microcontact, J. Colloid Interface Sci. 261 (2) (2003) 372–378, https://doi.org/10.1016/S0021-9797(03)00071-7, ISSN 0021-9797.
[73] W.R. Chang, I. Etsion, D.B. Bogy, Adhesion model for metallic rough surfaces, J. Tribol. 110 (1) (1988) 50–56, https://doi.org/10.1115/1.3261574, ISSN 0742-4787, 1528–8897.

[74] A. Ovcharenko, G. Halperin, I. Etsion, M. Varenberg, A novel test rig for in situ and real time optical measurement of the contact area evolution during pre-sliding of a spherical contact, Tribol. Lett. 23 (1) (2006) 55–63, https://doi.org/10.1007/s11249-006-9113-9, ISSN 1023-8883, 1573–2711.
[75] E. Rabinowicz, Influence of surface energy on friction and wear phenomena, J. Appl. Phys. 32 (8) (1961) 1440–1444, https://doi.org/10.1063/1.1728375, ISSN 0021-8979.
[76] R.G. Budynas, K. Nisbett, Shigley's mechanical engineering design, 10th ed., McGraw Hill, 2014.
[77] M.R.W. Brake, C.W. Schwingshackl, P. Reuß, On the observed variability and repeatability in jointed structures, Mech. Syst. Signal Process. 129 (2019) 282–307.
[78] B.J. Deaner, M.S. Allen, M.J. Starr, D.J. Segalman, H. Sumali, Application of viscous and Iwan modal damping models to experimental measurements from bolted structures, ASME J. Vib. Acoust. 137 (2015) 021012.
[79] D.J. Segalman, M.S. Allen, M. Eriten, K. Hoppman, Experimental assessment of joint-like modal models for structures, in: ASME International Design Engineering Technical Conferences IDETC/CIE, Boston, MA, 2015.
[80] C. Spearman, The proof and measurement of association between two things, Am. J. Psychol. 15 (1) (1904) 72, https://doi.org/10.2307/1412159, ISSN 00029556.
[81] R. Leach, Optical Measurement of Surface Topography, vol. 14, Springer, 2011.
[82] H.-J. Jordan, M. Wegner, H. Tiziani, Highly accurate non-contact characterization of engineering surfaces using confocal microscopy, Meas. Sci. Technol. 9 (7) (1998) 1142–1151, https://doi.org/10.1088/0957-0233/9/7/023, ISSN 0957–0233.
[83] D.A. Lange, H.M. Jennings, S.P. Shah, Analysis of surface roughness using confocal microscopy, J. Mater. Sci. 28 (14) (1993) 3879–3884, https://doi.org/10.1007/BF00353195, ISSN 1573-4803.
[84] R. Murthy, B.K. Choi, X.Q. Wang, M.C. Sipperley, M.P. Mignolet, C. Soize, Maximum entropy modeling of discrete uncertain properties with application to friction, Probab. Eng. Mech. 44 (2016) 128–137.
[85] X.Q. Wang, M.P. Mignolet. Stochastic Iwan-type model of a bolted joint: Formulation and identification. In 32nd International Modal Analysis Conference (IMAC XXXII), Orlando, FL, February 2014..
[86] M.P. Mignolet, C. Soize, Stochastic reduced order models for uncertain geometrically nonlinear dynamical systems, Comput. Methods Appl. Mech. Eng. 197 (2008) 3951–3963.